



HAL
open science

The Effect of a Weak Asthenospheric Layer on Surface Kinematics, Subduction Dynamics and Slab Morphology in the Lower Mantle

Nestor G. Cerpa, Karin Sigloch, Fanny Garel, Arnauld Heuret, D. Rhodri Davies, Mitchell Mihalynuk

► **To cite this version:**

Nestor G. Cerpa, Karin Sigloch, Fanny Garel, Arnauld Heuret, D. Rhodri Davies, et al.. The Effect of a Weak Asthenospheric Layer on Surface Kinematics, Subduction Dynamics and Slab Morphology in the Lower Mantle. *Journal of Geophysical Research: Solid Earth*, 2022, 127 (8), pp.e2022JB024494. 10.1029/2022JB024494 . hal-03764872

HAL Id: hal-03764872

<https://hal.umontpellier.fr/hal-03764872v1>

Submitted on 30 Aug 2022

HAL is a multi-disciplinary open access archive for the deposit and dissemination of scientific research documents, whether they are published or not. The documents may come from teaching and research institutions in France or abroad, or from public or private research centers.

L'archive ouverte pluridisciplinaire **HAL**, est destinée au dépôt et à la diffusion de documents scientifiques de niveau recherche, publiés ou non, émanant des établissements d'enseignement et de recherche français ou étrangers, des laboratoires publics ou privés.

1 **The effect of a weak asthenospheric layer on surface**
2 **kinematics, subduction dynamics and slab morphology**
3 **in the lower mantle**

4 **Nestor Cerpa¹, Karin Sigloch², Fanny Garel¹, Arnaud Heuret³, D. Rhodri**
5 **Davies⁴, Mitchell G. Mihalynuk⁵**

6 ¹Geosciences Montpellier, University de Montpellier, CNRS, Université des Antilles, Place Eugène
7 Bataillon, 34095 Montpellier, France

8 ²Geoazur, Université Côte d'Azur, CNRS, Observatoire de la Côte d'Azur, IRD, 250 Avenue Albert
9 Einstein, 06560 Valbonne, France

10 ³Université de Guyane, Géosciences Montpellier, 97300, Cayenne, France

11 ⁴Research School of Earth Sciences, The Australian National University, Canberra, ACT, 2601, Australia

12 ⁵British Columbia Geological Survey, PO Box 9333 Stn Prov Govt, Victoria, British Columbia V8W 9N3,
13 Canada

14 **Key Points:**

- 15 • Tectonic plate kinematics and seismic tomography suggest slab accumulation in
16 the mantle transition zone, beneath near-stationary trenches.
- 17 • By contrast, subduction dynamics models tend to produce inclined, laterally ex-
18 tended slabs associated with slab rollback and trench retreat.
- 19 • Adding a sub-lithospheric weak layer accelerates subduction, limits trench migra-
20 tion, and promotes sub-vertical slab piles, as observed.

Corresponding author: Nestor Cerpa, nestor.cerpa@umontpellier.fr

Abstract

On Earth, the velocity at which subducting plates are consumed at their trenches (termed ‘subduction rate’ herein) is typically 3 times higher than trench migration velocities. The subduction rate is also 5 times higher than estimated lower mantle slab sinking rates. Using simple kinematic analyses, we show that if this present-day “kinematic state” operated into the past, the subducting lithosphere should have accumulated and folded beneath near-stationary trenches. These predictions are consistent with seismic tomography, which images localized and widened lower-mantle slab piles. They are, however, at odds with most dynamic-subduction models, which predict rapid trench retreat and inclined slabs in the mantle transition zone. We test the hypothesis that a weak asthenospheric layer (WAL), between the lithosphere-asthenosphere boundary and 220 km depth, compatible with geophysical constraints, can remedy the discrepancies between numerical models and observations. The WAL lubricates the base of the lithosphere, increases the subduction rate while reducing trench retreat. As a consequence, simulations featuring a WAL predict slab accumulation at the mantle transition zone, and thicker, folded slabs in the lower mantle. A WAL viscosity only 2-5 times lower than that of the adjacent mantle is sufficient to shift subduction regimes towards a mode of vertical slab sinking and folding beneath near-stationary trenches, across a wide range of model parameters, producing surface and slab velocities close to those observed at the present-day. These findings provide support for the existence of a weak asthenosphere beneath Earth’s lithosphere, complementing independent evidence from various geophysical data.

Plain Language Summary

At convergent margins (subduction zones, marked by deep trenches), oceanic (subducting) plates plunge into Earth’s mantle. Analysis of the present-day surface velocities suggest that subducting plates are consumed at trenches at rates of 5 cm/yr, on average. Moreover, it is observed that the consumption rate is higher than the trench migration velocity, which is often less than 1 cm/yr. At depth below 660 km, marking the transition from the upper to the lower mantle, the subducted piece of the plate (the slab) encounters increased resistance to its sinking, with slab sinking velocities at these depths being less than about 1.5 cm/yr. Take together, such rapid plate consumption at quasi-fixed trenches, along with slab deceleration in the lower mantle, causes a “traffic jam” leading to sub-vertical accumulation of the slab and folding. This behavior is confirmed

53 by seismic imaging techniques of Earth's interior which reveals vertically-sinking piles
54 of oceanic slabs at and beneath a 660-km depth. However, computational and labora-
55 tory models of subduction zones often fail to reproduce these first-order observations.
56 Here, we demonstrate that the addition of a lubricating mantle layer at the base of the
57 oceanic plates reduces the mismatch between the aforementioned observations and pre-
58 dictions from 2-D computation models.

59 1 Introduction

60 The negative buoyancy of subducting plates is a primary driving force sustaining
 61 subduction and surface plate motions (Forsyth & Uyeda, 1975). Subduction zones are
 62 the sites of tectonically-forced horizontal deformation (Uyeda & Kanamori, 1979; Lalle-
 63 mand et al., 2005) and dynamic vertical motions (G. Davies, 1981; Gurnis, 1993). Crust
 64 and lithosphere subducting beyond the mantle transition zone add chemical heterogeneities
 65 to the lower mantle, which are stirred and homogenised by mantle convection (Zindler
 66 & Hart, 1986; Jones et al., 2016), or persist to the core-mantle-boundary, as suggested
 67 by modern tomographic models (e.g. Hosseini et al., 2020). Understanding the deep dy-
 68 namics of subducting slabs is thus key for addressing the geodynamical and geochem-
 69 ical evolution of our planet.

70 Observed plate kinematics provide insights into the dynamics of the subduction sys-
 71 tem (Forsyth & Uyeda, 1975; Jarrard, 1986; Lallemand et al., 2005; Heuret & Lallemand,
 72 2005; Sdrolias & Müller, 2006; Doglioni et al., 2007; Funiciello et al., 2008; Schellart, 2008b;
 73 Becker & Faccenna, 2009; Goes et al., 2011). Subduction kinematics (see Fig. 1) involve
 74 the velocities of the subducting plate v_{sp} (“SP velocity” for short); the velocity of the
 75 overriding plate v_{op} (“OP velocity”); and the velocity of the trench v_t , which is equal to
 76 OP velocity if the overriding plate does not undergo (back-arc) deformation. Note that
 77 v_{sp} and v_t are defined with opposite signs: the natural (positive) direction of trench mi-
 78 gration is “retreat” towards the SP. These absolute velocities are given in some absolute
 79 reference frame, which is taken as the stable lower mantle herein (Becker & Faccenna,
 80 2009).

81 The subduction rate v_s is the velocity of the subducting plate relative to the trench
 82 (i. e., the rate at which the subducting plate is consumed by the migrating trench). It
 83 has been repeatedly shown that typical values of v_s on Earth are higher than 3-4 cm/yr
 84 (Forsyth & Uyeda, 1975; Jarrard, 1986), while absolute trench motions are usually be-
 85 tween -2 and 2 cm/yr (Heuret & Lallemand, 2005; Funiciello et al., 2008; Schellart, 2008b).
 86 Other studies have pointed out that the magnitude of the (absolute) SP velocity v_{sp} is
 87 generally two to three times higher than that of the (absolute) v_t (Becker & Faccenna,
 88 2009; Goes et al., 2011; Carluccio et al., 2019). Hence plates are consumed at much faster
 89 rates than their trenches move laterally.

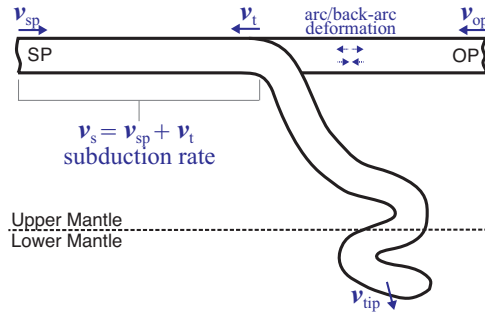


Figure 1. a) Sketch illustrating the various kinematics that can be inferred within a subduction system. Positive values denote absolute trenchward motion for both the subducting plate (v_{sp}) and the overriding plate (v_{op}). Absolute trench velocity (v_t) is considered positive towards the subducting plate. We define relative to a fixed lower-mantle reference frame, in order to compare to absolute motions in nature, which can be quantified in empirical, approximate mantle reference frames, such as the fixed-hotspot frame. Subduction velocity (v_s) is a relative velocity, the rate at which the subducting plate is consumed at the trench ($v_s = v_{sp} + v_t$).

90 Analogue and numerical models of subduction dynamics without external forcing
 91 (hereafter simply referred to as models of subduction dynamics) have shed light on the
 92 internal force balance of subduction systems and the resulting kinematics. They have
 93 illuminated various subduction regimes and slab morphologies in the upper mantle (e. g.
 94 Guillou-Frottier et al., 1995; Schellart, 2008a; Di Giuseppe et al., 2008; Ribe, 2010; Stegman
 95 et al., 2010). Recent studies that included an overriding plate with finite strength, con-
 96 cluded that the slab pull force associated with the negative buoyancy of a subducting
 97 plate (SP) favored slab rollback and migration of the trench towards the subducting plate
 98 (i. e., trench retreat), unless the SP was weak and/or the overriding plate (OP) was strong
 99 (Garel et al., 2014; Sharples et al., 2014; A. Holt et al., 2015; Hertgen et al., 2020). It
 100 has been pointed out that such analogue and numerical models of subduction dynam-
 101 ics tend to produce surface kinematics that are at odds with some of the first-order ob-
 102 servations outlined above (Goes et al., 2011; Carluccio et al., 2019). These subduction
 103 models generally produce trench retreat velocities that exceed present-day observations,
 104 especially once the subducting slab reaches the bottom of the upper mantle, which was
 105 sometimes treated as a rigid barrier (Funicello et al., 2004; Schellart, 2005; Capitanio
 106 et al., 2007; Goes et al., 2011). More modest trench motions over a relatively wide range
 107 of parameters have only been produced by 2-D models that consider both the penetra-

108 tion of the subducting slab into the lower mantle and complex rheologies (Garel et al.,
 109 2014; A. Holt et al., 2015; Z.-H. Li et al., 2019). Even then, slower trench motion is only
 110 achieved at the cost of decreasing the SP velocity to values of less than 2 cm/yr once the
 111 slab interacts with the viscosity increase around 660-km depth (hereafter referred to as
 112 “first slab-660 interaction”) (e.g. Garel et al., 2014; Suchoy et al., 2021). Hence, in most
 113 subduction dynamics models, more than half of the subduction rate v_{sp} is accounted for
 114 by trench motion v_t , which contradicts present-day observations of plate kinematics.

115 Independent constraints on subduction dynamics come from seismic tomographic
 116 images of slab morphologies at and below the mantle transition zone. A few slabs un-
 117 der present-day subduction zones in the Western Pacific appear to stagnate above the
 118 660-km discontinuity (Karason & Van Der Hilst, 2000; Amaru, 2007; C. Li et al., 2008;
 119 Fukao & Obayashi, 2013) - for instance, under Japan (Fukao et al., 1992) and under Izu-
 120 Bonin (Wu et al., 2016), at least under its northernmost part (Zhang et al., 2019). But
 121 many other slabs have breached the 660-km discontinuity and are sinking into the lower
 122 mantle (Goes et al., 2017). Transition-zone and lower-mantle slabs are imaged more ro-
 123 bustly and consistently than slabs in the upper(most) mantle. The opposite would be
 124 expected if slabs retained a constant thickness across depths. Hence the deeper slab must
 125 be thicker (Ribe et al., 2007; Loiselet et al., 2010), which is well-documented under the
 126 Americas (Karason & Van Der Hilst, 2000; Ren et al., 2007; Sigloch & Mihalynuk, 2013;
 127 Mohammadzaheri et al., 2021), but also globally (Van der Voo et al., 1999; Shephard et
 128 al., 2017; Van der Meer et al., 2018; Hosseini et al., 2020). Under the particularly well-
 129 instrumented Cascadia subduction zone of North America, tomography can resolve a shal-
 130 low slab of single lithospheric thickness, and also confidently show that the slab is mul-
 131 tiple thickened from the transition zone downward (Sigloch et al., 2008).

132 Thickened slabs in the lower mantle have been attributed to slab buckling and fold-
 133 ing through the mantle transition zone (Ricard et al., 1993; Guillou-Frottier et al., 1995;
 134 Ribe et al., 2007; Běhouňková & Čížková, 2008; Lee & King, 2011; Cerpa et al., 2014;
 135 Billen & Arredondo, 2018), with possible slab detachment (Čížková et al., 2012). Slab
 136 folds have not yet been resolved by tomography, so the exact widening mechanism re-
 137 mains speculative from the observational side.

138 Some numerical subduction models have produced vertical slab folding by impos-
 139 ing a fixed overriding plate, i.e., trench velocity $v_t = 0$ (e.g. Lee & King, 2011). Mod-

140 els with mobile plates often predict trench-retreat modes while sub-vertical slab folding
 141 tends to be limited to simulations with relatively young subducting plates and old over-
 142 riding plates (Garel et al., 2014; T. Yang et al., 2018; Strak & Schellart, 2021; Behr et
 143 al., 2022), or to double-subduction set-ups (Čížková & Bina, 2015; Lyu et al., 2019). By
 144 contrast, the tomographic observations – of pervasively thickened lower-mantle slabs, con-
 145 centrated in narrow, linear belts – suggest that slab folding beneath largely stationary
 146 trenches should prevail across a wide range of subduction settings. Thus we argue that
 147 current subduction models may lack a first-order ingredient that favors (almost) verti-
 148 cally stacked, thick lower-mantle slabs, which tends to be observed independently of plate
 149 strength and/or the distance to other subduction zones. Phase transitions at 410 and
 150 660 km can produce realistic lower-mantle slab morphologies by altering slab sinking rates
 151 (Briaud et al., 2020; Čížková & Bina, 2013; Arredondo & Billen, 2017), although the re-
 152 quired Clapeyron slopes may be too extreme (see e.g. Agrusta et al., 2017, and refer-
 153 ences therein). Hence there is room for considering alternative mechanisms.

154 To summarize, there are at least two discrepancies between existing models of sub-
 155 duction dynamics and first-order observations. First, current models generally produce
 156 trench retreat velocities v_t in excess of those observed at present-day subduction zones,
 157 alongside SP velocities v_{sp} and subduction rates v_s that are too slow after first slab-660
 158 interaction. Second, models seldom reproduce the tomographically observed, multiply
 159 thickened geometries that prevail in the transition zone and lower mantle.

160 This study considers how a weak asthenospheric layer (WAL) beneath the plate
 161 can resolve these discrepancies. The presence of a WAL on Earth has been proposed to
 162 explain a large range of geophysical observations, including lithospheric net rotation (Ricard
 163 et al., 1991), postglacial rebound and gravity data (e.g. Paulson & Richards, 2009), shear-
 164 wave tomography (Kawakatsu et al., 2009; Barruol et al., 2019), seismic attenuation (Y. Yang
 165 et al., 2007; Debayle et al., 2020), seismic anisotropy (Montagner & Tanimoto, 1991; De-
 166 bayle & Ricard, 2013; Becker, 2017) and electrical conductivity tomography (Naif et al.,
 167 2013). The viscosity reduction could originate from a plume-fed asthenosphere (Phipps Mor-
 168 gan et al., 1995), from the depth-dependency of dislocation creep flow laws (Raterron
 169 et al., 2011), from crystal-preferred orientation (Meyers & Kohlstedt, 2021), or from the
 170 presence of melt pockets (Cooper & Kohlstedt, 1986; Chantel et al., 2016), which may
 171 remain trapped due to low melt fractions (Holtzman, 2016) or low density contrast (Sakamaki
 172 et al., 2013).

173 The presence of a WAL is predicted to affect large-scale dynamics of the underly-
 174 ing, convecting mantle (Lenardic et al., 2006), and to favor ‘plate-like’ rather than ‘stagnant-
 175 lid’ regimes (Höink et al., 2012). Since the sub-lithospheric mantle resists a plate’s trench-
 176 ward motion, the inclusion of a WAL in models of subduction dynamics yields faster sub-
 177 duction velocities v_{sp} , as shown by Carluccio et al. (2019) and Suchoy et al. (2021). The
 178 latter authors also showed that increased v_{sp} was coeval with reduced trench retreat v_t ,
 179 although they did not detail the implications for lower mantle slab morphologies. We
 180 hypothesize that increasing subduction rates while reducing trench motion results in the
 181 accumulation of slab material in a near-vertical column beneath the (quasi stationary)
 182 trench, and that the slab must widen (through folding) around the depths where it slows
 183 down to lower-mantle sinking rates, given that slab input v_s remains high. Thus, a WAL
 184 could resolve both first-order discrepancies regarding plate velocities and slab morpholo-
 185 gies.

186 We carry out a systematic numerical analyses of how a WAL impacts the dynam-
 187 ics of thermo-mechanical subduction models featuring an overriding plate. Section 2 pro-
 188 vides a first-order quantification of slab widening behavior in modern subduction zones,
 189 using plate kinematic data. Section 3 describes the model setup. Section 4 presents our
 190 modeling results, and Section 5 discusses their implications for subduction systems on
 191 Earth.

192 **2 Quantifying slab folding from plate motions and slab sinking rates**

193 **2.1 Conceptual assessment**

194 We start by demonstrating how slab folding can be assessed theoretically as a ge-
 195 ometrical/kinematic phenomenon, involving slab accumulation in the mantle transition
 196 zone. This analysis is inspired by subduction models where (unlike our own model) ve-
 197 locities are applied to one or both plates, and which can predict slab morphology as a
 198 function of these imposed surface kinematics (Christensen, 1996; Heuret et al., 2007; Ar-
 199 cay et al., 2008; Gibert et al., 2012; Cerpa et al., 2015; Guillaume et al., 2018; Cerpa et
 200 al., 2018). Among these, Gibert et al. (2012), anchored the subducting slab to a rigid
 201 660-km discontinuity, which aims to simulate the effect of a strong viscosity jump at 660
 202 km, as inferred from e.g. geodetic constraints (B. H. Hager, 1984; B. Hager & Richards,
 203 1989; Mitrovica & Forte, 2004). Gibert et al. (2012) showed that if the subduction rate

204 $v_s = v_{sp} + v_t$ exceeds the trench velocity v_t , continued subduction results in slab fold-
 205 ing at the base of the upper mantle. Essentially, the slab has to fold because trench re-
 206 treat does not create enough lateral accommodation space to permit all incoming slab
 207 to lie down flat on the '660'. Here we extend their analysis to the more general case where
 208 the subducting slab sinks into the lower mantle.

209 Let $v_s \times \Delta t$ be the length of subducted material consumed at the trench over some
 210 duration Δt . The lateral displacement of the trench over the same duration is $v_t \times \Delta t$.
 211 The displacement of the deepest portions of the subducting slab (simplified as the dis-
 212 placement of the slab tip) within the upper mantle is approximated as $v_{\text{tip}} \times \Delta t$, where
 213 v_{tip} is the absolute velocity of the deepest point of the slab. Slab folding can thus be
 214 understood as a simple geometrical constraint. When the length of subducted material
 215 is larger than the lateral displacement of the trench plus the displacement of the slab tip,
 216 the excess length (slab accumulation) is expected to be accommodated by folding. Put
 217 in another form, slab accumulation and folding occurs when:

length of subducted material > trench displacement + slab tip motion in the mantle

218 Alternatively, we can define a kinematic ratio K_r which predicts whether the sub-
 219 ducting slab undergoes folding as:

$$K_r = \frac{v_s}{|v_t| + \sqrt{(v_{\text{tip}}^x)^2 + (v_{\text{tip}}^z)^2}} \quad (1)$$

220 where we have decomposed the velocity of the deepest point of the slab into its horizon-
 221 tal and vertical components.

222 When $K_r \simeq 1$, the free space created by trench retreat and slab sinking can ac-
 223 commodate all newly incoming lithosphere, which does not have to compress (fold). Hence
 224 the slab's apparent thickness remains similar in the upper and lower mantle (Fig. 2). A
 225 kinematic ratio K_r higher than 1 implies a surplus of slab material that cannot be ac-
 226 commodated by trench retreat and slab sinking into the lower mantle, and instead has
 227 to be accommodated by slab folding. At $K_r > 1$, the higher the value of K_r , the greater
 228 the frequency of slab folds (or alternatively, the wider the amplitude of the folds). Also
 229 at $K_r > 1$, the apparent thickness of the folded slab in the lower mantle is predicted
 230 to be multiples of the lithospheric thickness observed in the uppermost mantle.

231 The ratio of trench velocity to slab-sinking velocity (v_t/v_{tip}^z) controls, to first or-
 232 der, the average slab dip. This is true for both the unfolded ($K_r \leq 1$) and folded ($K_r >$

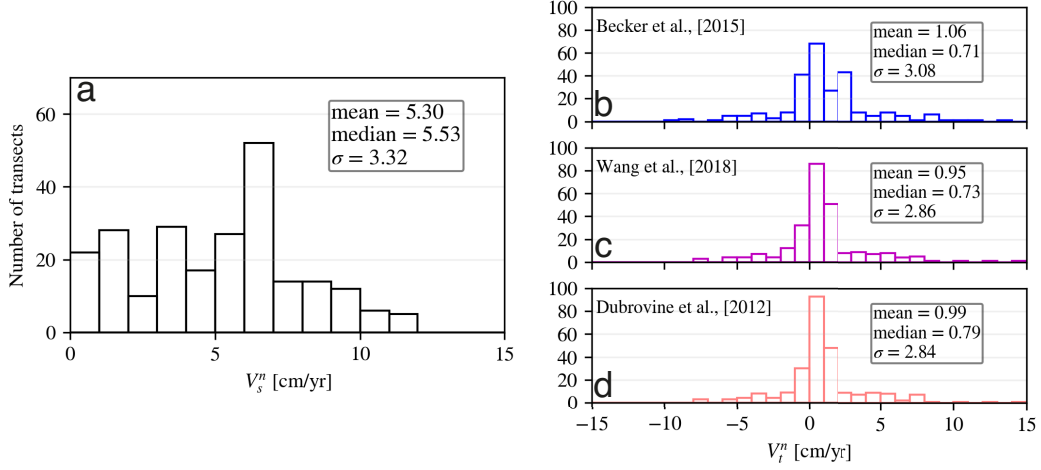


Figure 2. Range of theoretically possible geometries for slabs that sank vertically after entering the trench and have penetrated well into the lower mantle (LM). Dashed lines mark the viscosity discontinuity between upper mantle (UM) and LM, in this study assumed to equate to the seismic “660-km discontinuity”. The x-axis plots the ratio of trench motion to the slab’s (approximate) sinking velocity. v_t is absolute trench velocity and v_{tip}^z is the vertical velocity component of the deepest slab tip (approximating the slab’s overall sinking rate). Positive values of v_t/v_{tip}^z represent trench retreat, negative values trench advance. A stationary trench ($v_t/v_{tip}^z = 0$) leads to a vertical slab piling up beneath it; a migrating trench results in a dipping slab. The y-axis plots the kinematic ratio (K_r , Eq. 1) which expresses whether the length of slab newly entering the mantle (per time unit) can be accommodated in the slab-free space created by trench migration (horizontally away from the slab) and/or by the sinking of older motion of the slab (which vacates upper-mantle space). $K_r > 1$ indicates a shortfall of newly created accommodation space, so that the slab must fold (or thicken in some other way) in order to adjust.

233 1) cases. Note that we use only the vertical component of the slab-tip velocity as it is
 234 thought to be much higher than the horizontal component (see also below section 2.2).

235 Hence the parameter space along the dimensions of K_r and v_t/v_{tip}^z spans a vari-
 236 ety of candidate slab morphologies and subduction regimes, as depicted in (Fig. 2). For
 237 negative trench motion (trench advance), the subducting slab leans forward, so that the
 238 deepest slab portions lie beneath the subducting plate at increasing distances from the
 239 trench (leftmost regimes in Fig. 2). For quasi-null trench motions, the subducting slab
 240 sinks vertically, with all slab portions remaining below the trench. For relatively high,

241 positive trench motions (trench “retreat”), the subducting slab leans backwards (“slab
 242 rollback”), with deeper slab beneath the overriding plate. It has been proposed that high
 243 trench-retreat rates promote the complete stagnation of slab atop the 660-km discon-
 244 tinuity (Torii & Yoshioka, 2007; Goes et al., 2017), so that high values of v_t/v_{tip}^z may
 245 lead to the end-member subduction regime where the slab flattens and folds on the 660-
 246 km discontinuity (rightmost regimes in Fig. 2).

247 **2.2 Estimating slab folding at present-day**

248 In order to gauge the prevalence of slab folding in nature, we seek to calculate an
 249 observational estimate of K_7 in active subduction zones, using Equation 1. Hence we need
 250 estimates of subduction rate v_s , absolute trench velocity v_t , and slab sinking velocity v_{tip} .

251 For estimating v_s and v_t , we use an updated version of the SUBMAP database (Lallemand
 252 et al., 2005), which defines 249 transects of active subduction zones. Subduction rates
 253 are retrieved from the relative plate motions of the MORVEL56-NNR model (based on
 254 a circuit of 56 tectonic plates (Argus et al., 2011) as explained in the Supplementary In-
 255 formation Text S1). Each SUBMAP subduction transect is assigned to a subducting plate
 256 and an overriding plate of the MORVEL56-NNR plate circuit. For transects that cross
 257 significant arc and back-arc deformation, MORVEL56-NNR permits the definition of an
 258 “arc block” and assessment of trench motion relative to that of a rigid overriding plate,
 259 enhancing the accuracy of the derived subduction rate. For a few subduction zones, the
 260 MORVEL56-plate circuit does not account for active arc and back-arc deformation even
 261 though such a deformation has been well-established in the literature (Southernmost-
 262 Central Andes, Izu-Bonin, Calabria). For these transects, we complement MORVEL56-
 263 NNR with published regional studies (see Supplementary Information).

264 To define the absolute motion of the plates and trenches, we need to consider an
 265 absolute plate motion model within an absolute reference frame, comparable to the fixed
 266 reference frame of our numerical models. In this paper we calculate and compare the value
 267 of K_7 in three recent absolute plate motion models, constructed in different manners:
 268 the “SA” (“spreading-alignment”) model (Becker et al., 2015), the “TM25” model (Wang
 269 et al., 2018), and the “GMHRF-1Ma” model by Doubrovine et al. (2012). The SA model
 270 minimizes the angular misfit between spreading-ridge orientations and plate velocities.
 271 This plate motion was found to give a good fit to azimuthal seismic anisotropy, a proxy

272 for the shear induced by the relative motion between the tectonic plates and the upper
 273 mantle. The TM25 model is based on 25 hotspot tracks under the assumption of fixed
 274 hotspots relative to the deep mantle. The GMHRF-1Ma model is based on a global fit
 275 of hotspot tracks since the Late Cretaceous, accounting for modest relative motions be-
 276 tween the hotspots' mantle plumes, computed by numerical models of whole mantle con-
 277 vection.

278 We extract the trench-normal component of the plates and trench velocities for com-
 279 parison with our 2-D models. In what follows, the absolute and relative velocities at each
 280 transect are those of their trench-normal components.

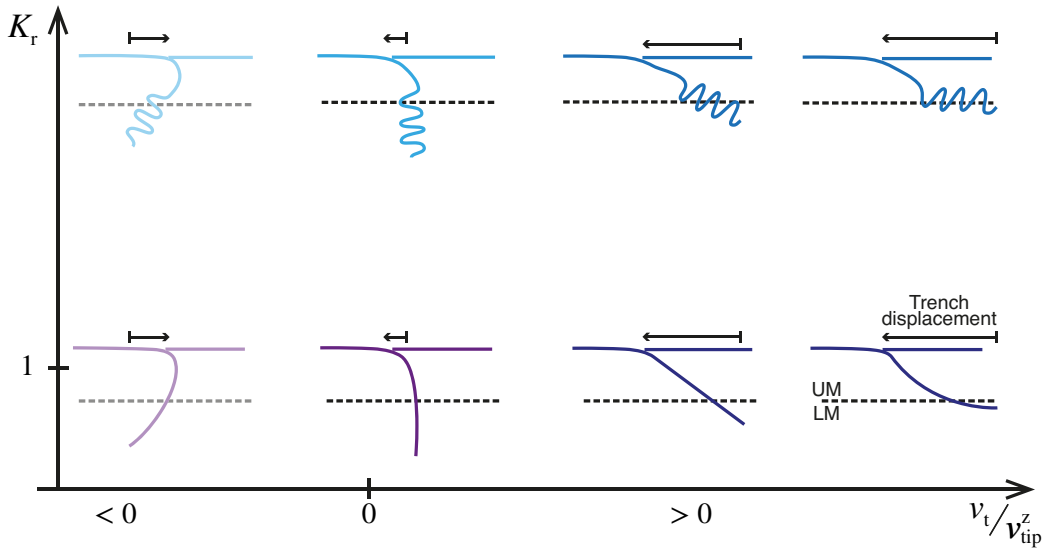


Figure 3. a) Histogram of the trench-normal component of subduction rate v_s in present-day subduction zones. b) Histogram of the trench-normal component of trench velocity (retreat) v_t , in the spreading-alignment reference frame (Becker et al., 2015). c) Histogram as in b) but for T25M reference frame (Wang et al., 2018). d) Like b), but for GMHRF-1Ma frame (Dobrovine et al., 2012).

281 The observed subduction rates are non-negative with a median value of 5.3 cm/yr
 282 and a long tail up to almost 12 cm/yr (Fig. 3a). In all three reference frames (Fig. 3b-
 283 d), absolute trench velocity v_t scatters around slightly positive values with a median val-
 284 ues of 0.71 to 0.79 cm/yr. This tendency towards slow trench retreat may or may not
 285 be significantly different from zero motion (stationary trench), given the large formal stan-
 286 dard deviations of almost 3 cm/yr but also the non-Gaussian, heavy tails of the histogram.

287 In any case, two thirds of the subduction transects have trench velocities between -1 and
 288 1 cm/yr in the three absolute plate motion frames. Hence typical present-day trench mo-
 289 tion is roughly five times smaller than typical subduction velocities.

290 Estimating K_r also requires an estimate of slab sinking rates in the lower mantle.
 291 In principle, the reduction of slab sinking rate from UM to LM could be derived from
 292 the viscosity contrast between upper and lower mantle (Richards, 1991; Ricard et al.,
 293 1993). Given the rheology uncertainties and variability of slab sinking rates across the
 294 upper mantle, we prefer to use estimates based on tomographic observations. Since im-
 295 aged slabs are not directly dateable, they have been correlated to the geology of accre-
 296 tionary orogens, which hold the surface record of subduction. The subduction of litho-
 297 sphere is accompanied by the formation of a volcanic arc at the surface, which often sur-
 298 vives and is dateable. Such slab-arc correlations have inferred time-averaged sinking rates
 299 of 1.0-1.5 cm/yr for slabs that have penetrated the lower mantle (Van Der Meer et al.,
 300 2010; Sigloch & Mihalynuk, 2013; Domeier et al., 2016; Van der Meer et al., 2018; Mo-
 301 hammadzaheri et al., 2021).

302 Using 1.0 cm/yr as the slab sinking velocity estimate, 70–80% of subduction tran-
 303 sects exhibit values of $K_r > 1$ in all three absolute reference frames (Fig. 4 and Fig.
 304 S1). Only a few subduction transects consistently display $K_r < 1$ in all reference frames,
 305 mostly at the edges of longer arcs: the southernmost Andes (Patagonian transects), the
 306 northern edge of the Lesser Antilles (e.g. Puerto Rico Trench), or the edges of the South
 307 Sandwich SZ.

308 The present-day prevalence of $K_r > 1$ is relatively insensitive to the assumed slab
 309 sinking velocity. Even when considering $v_{tip} = 1.5$ cm/yr, at the high end of the rea-
 310 sonable estimate range (see e.g. Butterworth et al., 2014; Domeier et al., 2016)), 63%
 311 of transects remain above $K_r > 1$ in the spreading-aligned absolute plate motion model,
 312 and 72% of transects in the two other reference frames.

313 Figure 4a plots the global inventory of slabs (between 600-1800 km depth), from
 314 which the sinking rates were derived. Importantly, most areas are slab free. Existing slabs
 315 cluster in two vast, linear belts: one under the Alpine-Eurasian-Himalayan-southwest Pa-
 316 cific orogens; the second under the Americas and into Siberia. From the geologic record
 317 and quantitative plate reconstructions, these are the known, absolute locations of ma-
 318 jor orogenies over the past 200 million years, hence the known paleo-trench locations.

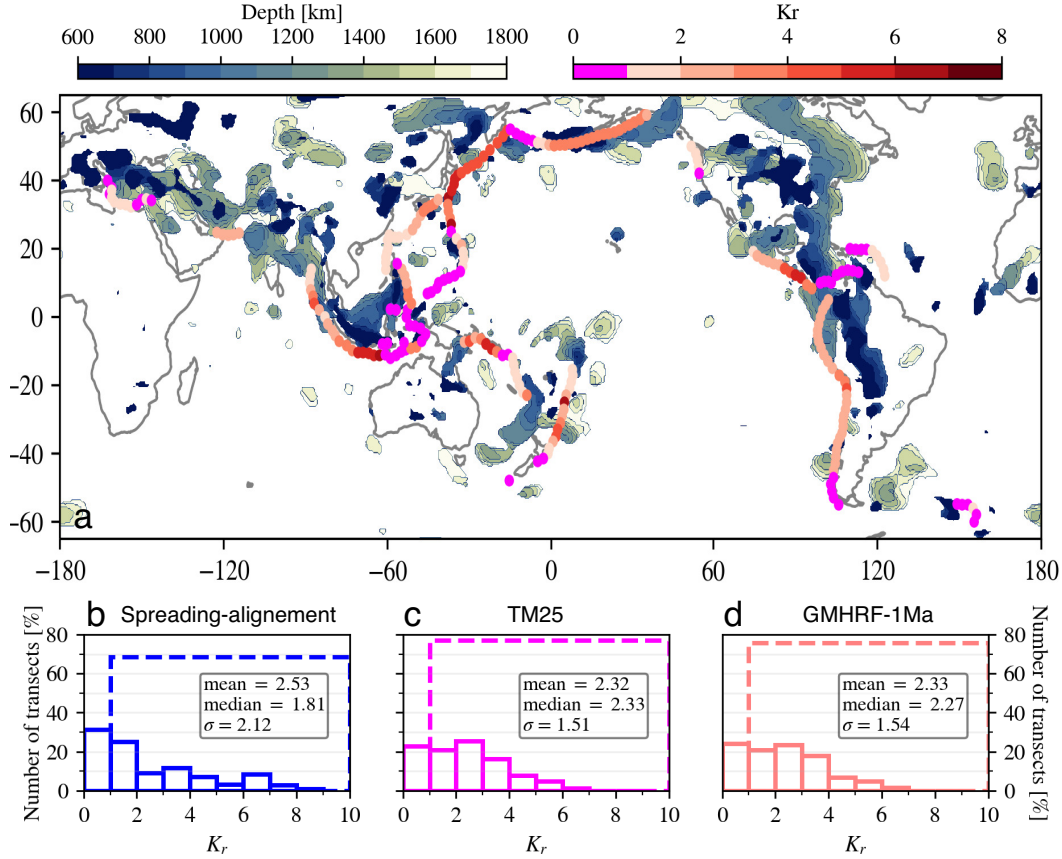


Figure 4. a) Map shows estimates of the kinematic ratio K_r (reddish color scale) for all subduction transects of the SUBMAP database (Heuret & Lallemand, 2005). The regime of inferred slab folding ($K_r > 1$) prevails in most subduction zones. The absolute plate motion model is GMHRF-1Ma, which yields intermediate K_r values compared to the also-investigated spreading-alignment and TM25 models (plotted on Fig. S1 in the supplementary information). Also shown in blue shades is the global inventory of subducted slabs in the lower mantle (600-1800 km depth). More precisely, these are contours of seismically fast P-velocity anomalies exceeding $dvp/vp > 0.35\%$ in global model DETOX-P2 (Hosseini et al., 2020). b) Histogram of K_r values in the spreading-alignment reference frame. c) Histogram of K_r values in the TM25 reference frame. d) Histogram of K_r values in the GMHRF-1Ma reference frame.

319 The observation that slabs are still located only beneath these independently inferred
 320 paleo-trench regions means that slabs sank rather vertically. The vast slab-free mantle
 321 areas are known not to have hosted trenches over the past 200 m.y. This implies that
 322 paleo-trenches have remained quite stationary over a time period during which the area
 323 equivalent of all ocean basins was subducted once or twice over (Coltice et al., 2012). Thus

324 trenches had the opportunity to migrate across the globe but did not, which indicates
 325 sustained $K > 1$ (slab folding regime) over geologic time.

326 Finally, slab dimensions directly point towards folding. In figure 4a, the Eurasian
 327 and American slab belts are 15,000-20,000 km long; individual slab segments are 1,000-
 328 3,000 km long (i.e., arc length) and 400-700 km wide. The latter is a multiple of litho-
 329 spheric thickness, and suggests slab folds of this amplitude.

330 Thus three separate lines of observational reasoning suggest that most present and
 331 past subduction zones feature(d) a surplus of subducted material not accommodated by
 332 lateral trench migration and slab sinking, so that instead slab folding is required. As dis-
 333 cussed, common models of subduction dynamics (hereafter referred to as standard mod-
 334 els) seldom reproduce this regime. Next we investigate whether adding a WAL to a stan-
 335 dard model can shift its regimes from non-folding to folding over a wide range of model
 336 parameters.

337 **3 Modeling approach**

338 We use 2-D thermo-mechanical models of subduction dynamics. The governing equa-
 339 tions are those suitable for multi-material, incompressible viscous flow, under the Boussi-
 340 nesq approximation, which are solved using the finite-element, control-volume, unstruc-
 341 tured adaptive mesh Fluidity computational modelling framework, which has been care-
 342 fully validated for simulations of this nature (D. R. Davies et al., 2011; S. Kramer et al.,
 343 2012; Le Voci et al., 2014; S. C. Kramer et al., 2021). Our model setup and material prop-
 344 erties are similar to Garel et al. (2014), albeit that in some cases we extend the mod-
 345 els by incorporating a sub-lithospheric weak asthenospheric layer (WAL), similar to that
 346 in Suchoy et al. (2021). Our models neglect the potential effects of phase transitions on
 347 the buoyancy forces. Below we summarize our modeling approach.

348 **3.1 Model Setup**

349 The model predicts the evolution of a single subduction zone comprising both a
 350 subducting plate (SP) and an overriding plate (OP), with no external forces or veloc-
 351 ities applied to the system. The model domain is a Cartesian box that is 8000-km wide
 352 and 2900-km in height (i.e. the whole mantle depth). Mechanical boundary conditions
 353 on the sides and base of the domain are free-slip, with a free-surface at the top. We use

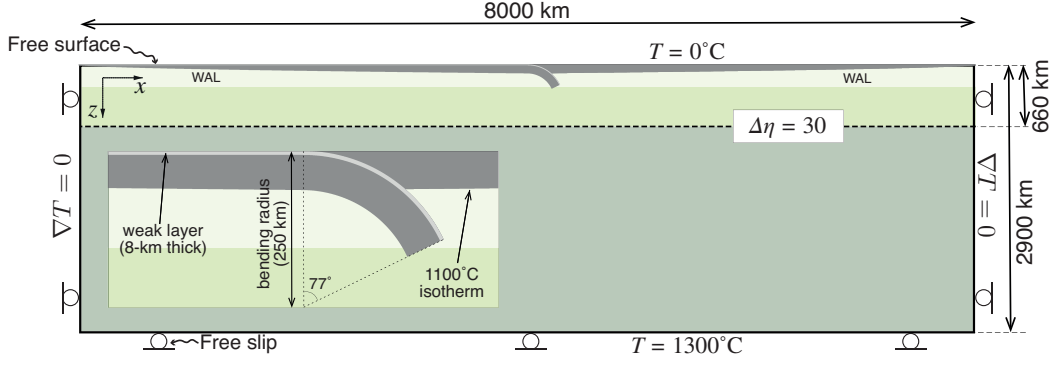


Figure 5. Model setup and boundary conditions. In the standard models the viscosity of the WAL is equal to that of ambient mantle ($\alpha = 1$), i.e., no weak asthenospheric layer (WAL) is present. The initial curved geometry of the subducting plate is prescribed using a bending radius of 250 km, including the weak layer.

354 no-flux thermal boundary conditions on the sides and impose constant temperatures of
 355 0°C and 1300°C at the surface and at the bottom boundaries, respectively.

356 The initial temperature field is given by a half-space cooling model where the age
 357 of the plates vary linearly from the 0 at the ridges to (A_{SP}) for the subducting plate and
 358 to (A_{OP}) for the overriding plate. Models begin with a curved subducting slab to ini-
 359 tiate subduction (see inset Fig. 5). Two mid-ocean ridges are initially set at either end
 360 of the model box, and are subsequently free to move according to the model dynamics.

361 We consider a composite visco-plastic rheology that accounts for four deformation
 362 mechanisms: linear diffusion creep, and non-linear dislocation creep, Peierls creep and
 363 pseudo-brittle yielding. The effective viscosity is:

$$\frac{1}{\eta_{eff}} = \left(\frac{1}{\eta_{diff}} + \frac{1}{\eta_{disl}} + \frac{1}{\eta_P} + \frac{1}{\eta_Y} \right) \quad (2)$$

364 which is bounded at lower (10^{18} Pa s) and upper (10^{25} Pa s) limits.

365 The diffusion (η_{diff}), dislocation (η_{disl}) and Peierls (η_P) viscosities follow the generic
 366 form:

$$\eta_{diff|disl|P} = A^{\frac{1}{n}} \exp\left(\frac{E + PV}{nRT_r}\right) \dot{\epsilon}_{II}^{\frac{1-n}{n}} \quad (3)$$

367 where A is a prefactor, n is the stress exponent, E and V are the activation energy and
 368 volume, respectively. P is the lithostatic pressure, R the gas constant, and $\dot{\epsilon}_{II}$ the sec-
 369 ond invariant of the strain-rate tensor. T_r is the sum of model temperature and an adi-

370 abatic temperature gradient of 0.5 °C/km and of 0.3 °C/km in the upper and lower man-
 371 tle, respectively. The pseudo-brittle yielding viscosity follows a yield-stress law

$$\eta_Y = \frac{\tau_Y}{2\epsilon_{II}} \quad (4)$$

372 where the yield strength $\tau_Y = \min(\tau_0 + f_c P, \tau_Y^{\max})$, with τ_0 the surface yield strength,
 373 f_c the friction coefficient, P the lithostatic pressure, and τ_Y^{\max} the maximum yield strength.
 374 The interface weak layer is 8-km thick, with a friction coefficient 10 times lower than the
 375 mantle material, and a maximum prescribed viscosity of 10^{20} Pa s. We impose a viscos-
 376 ity contrast $\Delta\eta$ of 30 at a 660-km depth between upper and lower mantle (B. H. Hager,
 377 1984; Gurnis & Hager, 1988; Ricard et al., 1993; Čadež & Fleitout, 1999; Mitrovica &
 378 Forte, 2004). All rheological parameters are listed in Table 1.

379 **3.2 Treatment of WAL**

380 The depth extent of a potential WAL is not well constrained. Some studies, which
 381 consider it to be a layer of partial melt, suggest that it is only 10-20 km thick (Schmerr,
 382 2012; Sakamaki et al., 2013; Stern et al., 2015), whereas others advocate for a layer ex-
 383 tending from the lithosphere-asthenosphere boundary up to 200-300 km depth (thus a
 384 thickness of approximately 100-200 km) (Kawakatsu et al., 2009; Paulson & Richards,
 385 2009; French et al., 2013; Becker, 2017; Barruol et al., 2019; Debayle et al., 2020). Here,
 386 we simulate the presence of the WAL by imposing a viscosity reduction between the 1100 °C
 387 isotherm (a proxy for the LAB) and a depth of 220 km, similarly to Suchoy et al. (2021).
 388 Note that models tested with a WAL extending up to 300 km depth showed little dif-
 389 ferences with the results reported below. We define the effective viscosity within the WAL
 390 as:

$$\eta_{\text{WAL}} = \alpha \eta_{\text{eff}} \quad (5)$$

391 where $0 < \alpha \leq 1.0$ is a reduction-viscosity factor.

392 The viscosity reduction of a WAL, and its origin, is also debated. For example, par-
 393 tial melt can lead to a 20-fold or larger viscosity reduction (Holtzman, 2016), but strongly
 394 depends on melt fraction, creep regime, grain size and wetting angle (Kohlstedt & Zim-
 395 merman, 1996). Milder viscosity reduction (< 5-fold) are expected from crystal-preferred
 396 orientation considerations (Meyers & Kohlstedt, 2021). We explore α values of 1.0 (no
 397 viscosity reduction – standard case); 0.5 (two-fold weaker asthenosphere – WAL case);
 398 and 0.2 (five-fold weaker – pronounced WAL case)). Note that larger viscosity reduc-

399 tions (α in the range 0.01–0.1) have usually been used in global mantle flow models re-
 400 producing sub-plate seismic anisotropy (Conrad & Behn, 2010; Becker, 2017). In our mod-
 401 els with a composite rheology, shearing in the sub-plate mantle produces additional weak-
 402 ening of the strained layer relative to the underlying ambient mantle, by the sole effect
 403 of dislocation creep. Thus a nominal reduction factor of $\alpha = 0.2$ to 0.5 may produce ac-
 404 tual viscosity reductions by one order of magnitude (see e.g. the viscosity profile in Fig.
 405 S10). Empirically, values of α lower than 0.1 in our set-up led to unrealistically large sur-
 406 face velocities >50 cm/yr very early in the simulations.

407 **4 Model results**

408 We first perform a set of simulations without a WAL ($\alpha = 1$), that we hereafter
 409 refer to as standard cases. Next, we explore sets of simulations with different degrees of
 410 weakening in the WAL (i.e. various values of α), that we refer to as WAL cases. For each
 411 case, we define a reference simulation (with plate ages $A_{sp} = 40$ My and $A_{op} = 20$ My).
 412 We subsequently run simulations that span a range of initial ages to cover a wide range
 413 of strength and buoyancy for both plates, while being representative of all regions of the
 414 subduction regime diagram presented in Garel et al. (2014).

415 **4.1 Standard cases - no WAL**

416 **4.1.1 Reference simulation [$A_{sp} = 40$ My; $A_{op} = 20$ My]**

417 Figure 6 displays the temporal evolution of the reference simulation for the stan-
 418 dard cases ($\alpha = 1$). We focus on the evolution of the surface kinematics and the vis-
 419 cosity field in the sub-plate mantle (i.e., the uppermost upper mantle which undergo rel-
 420 atively high shear stresses and which is found between the cold lithosphere and depths
 421 of up to a 300-km depth). The velocity profile along the plates corresponds to "plate-
 422 like behavior": the velocity is constant except in the trench region, where both plates
 423 undergo deformation (Figure S3). Since trench velocity is very similar to OP velocity,
 424 indicating little back-arc deformation at all stages of the models, we will only describe
 425 the evolution in terms of trench velocity.

426 During the first stage of free sinking through the upper mantle (Fig. 6a), the sub-
 427 ducting plate accelerates as slab pull increases with increasing slab length. It reaches a
 428 peak velocity of ~ 13 cm/yr with trench retreat/OP velocity peaking at ~ 4 cm/yr (Fig. 6g).

Table 1. Physical parameters used in the simulations, unless stated otherwise. UM and LM stand for upper and lower mantle, respectively.

Quantity	Symbol	Units	Value
Gravity	g	m s^{-2}	9.8
Thermal expansivity coefficient	α	K^{-1}	$3 \cdot 10^{-5}$
Thermal diffusivity	κ	$\text{m}^2 \text{s}^{-1}$	10^{-6}
Reference density	ρ_s	kg m^{-3}	3300
Cold, surface temperature	T_s	K	273
Hot, mantle temperature	T_m	K	1573
Gas constant	R	$\text{J K}^{-1} \text{mol}^{-1}$	8.3145
Max. viscosity	η_{max}	Pa s	10^{25} 10^{20} (WI)
Max. viscosity interplate layer	$\eta_{\text{max,weak}}$	Pa s	10^{20}
Min. viscosity	η_{min}	Pa s	10^{18}
<i>Diffusion creep</i>			
Activation energy	E	kJ mol^{-1}	300 (UM) 200 (LM)
Activation volume	V	$\text{cm}^3 \text{mol}^{-1}$	4 (UM) 1.5 (LM)
Prefactor	A	$\text{Pa}^{-1} \text{s}^{-1}$	$3.0 \cdot 10^{-11}$ (UM) $6.0 \cdot 10^{-17}$ (LM - $\Delta\eta = 30$)
	n	-	1
<i>Dislocation creep (UM)^a</i>			
Activation energy	E	kJ mol^{-1}	540
Activation volume	V	$\text{cm}^3 \text{mol}^{-1}$	12
Prefactor	A	$\text{Pa}^{-n} \text{s}^{-1}$	$5.0 \cdot 10^{-16}$
	n	-	3.5
<i>Peierls mechanism creep (UM)^a</i>			
Activation energy	E	kJ mol^{-1}	540
Activation volume	V	$\text{cm}^3 \text{mol}^{-1}$	10
Prefactor	A	$\text{Pa}^{-n} \text{s}^{-1}$	10^{-150}
	n	-	20
<i>Yield strength law</i>			
Surface yield strength	τ_0	MPa	2
Friction coefficient	f_c	-	0.2
	$f_{c,\text{weak}}$	-	0.02 (weak layer)
Maximum yield strength	$\tau_{y,\text{max}}$	MPa	10 000

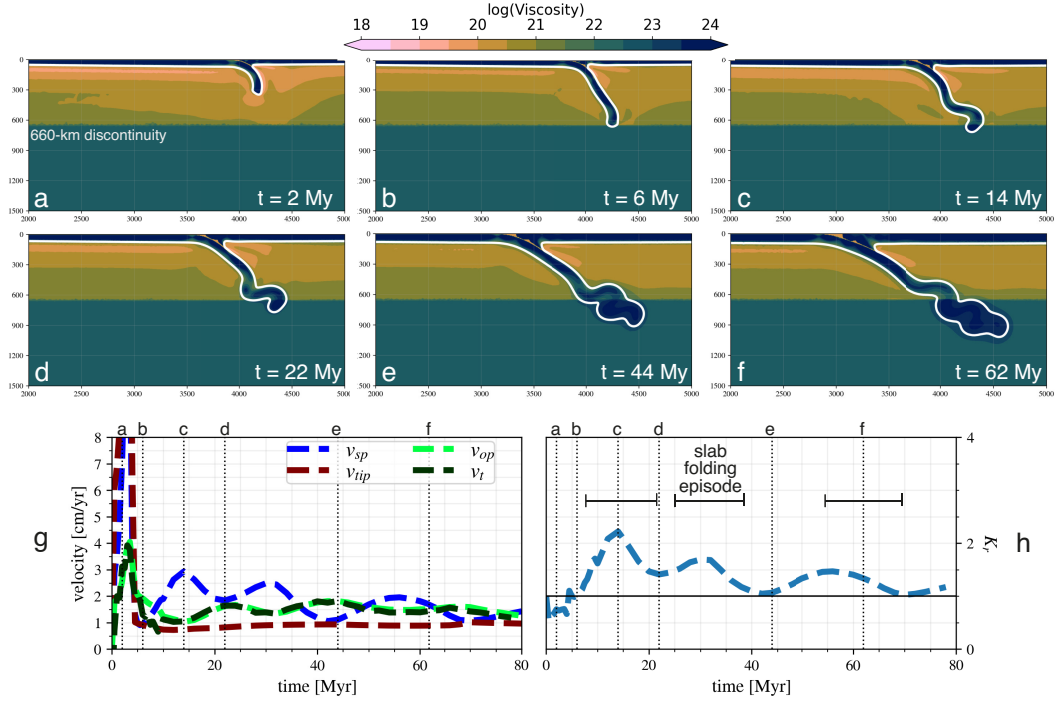


Figure 6. Reference standard model, featuring $A_{sp} = 40$ and $A_{op} = 20$ My. (a-f) Temporal snapshots of the evolution of the viscosity field, from 2 My to 62 My. The white line gives the 1100°C-isocontour. g) Kinematics of plates, slab, and trench. v_{sp} in dark blue, positive to the right. v_{op} in green, positive to the left. v_t in light blue, positive to the left. v_{tip} in dark red is the magnitude of slab tip velocity in. Vertical dashed lines mark snapshots times of (a-f). h) Temporal evolution of Kinematic ratio K_r , a proxy for the slab’s propensity to fold (definition in the text). Horizontal black line denotes the boundary between the folding ($K_r > 1$) versus non-folding ($K < 1$) regime.

429 The fast SP motion induces high shear stresses in the underlying asthenosphere. This
 430 causes high sub-plate strain rates, which favors dislocation creep and lower viscosity than
 431 in the less-sheared, underlying mantle. The same occurs within the mantle wedge be-
 432 low 200 km depth, where high strain rates are due to corner flow. Away from these high-
 433 strain rate regions, diffusion creep dominates (see e.g. Garel et al., 2014).

434 As soon as the slab tip encounters the high-viscosity lower mantle around $t \simeq 5$
 435 My, plate velocities decrease to between 1 and 3 cm/yr. The decreases in velocity and
 436 sub-plate shear lead to a slight increase of mantle viscosity beneath the subducting plate,

437 compared to the free-sinking stage. After the slab-660 interaction, the viscosity of the
 438 sub-plate mantle increases to typically above 10^{20} Pa s.

439 The slab-660 interaction is followed by two episodes of slab folding. First the slab
 440 bends with an OP-wards concavity between ~ 6 and ~ 14 My (Fig. 6b-c), with an increase
 441 in SP velocity (up to 3 cm/yr) and low trench velocity of approximately 1 cm/yr. Then
 442 a transient stage of slab rollback, associated with a slight increase in the trench veloc-
 443 ities up to 1.5 cm/yr, lasts for approximately 5 My (Fig. 6c) and lowers slab dip in the
 444 upper mantle. The second folding episode occurs between ~ 25 and ~ 40 My: the deeper,
 445 folded portion of the slab flattens above the lower mantle while the shallow slab contin-
 446 ues to roll back (Fig. 6d), increasing slab pull (v_{sp} up to ~ 2.5 cm/yr). Another tran-
 447 sient stage of trench retreat without buckling follows (Fig. 6e), with trench velocity (1.8
 448 cm/yr) greater than the SP velocity (1 cm/yr).

449 These two folding episodes are reflected in temporal changes in the viscosity of the
 450 sub-plate mantle. Its lowest strength is observed during the short SP-velocity peaks, es-
 451 pecially underneath the SP (see e.g. Fig. 6c). In contrast, the slight increases in trench/OP
 452 motion appear to have little effect on the viscosity field beneath the OP. The highest val-
 453 ues of sub-plate mantle viscosity are in fact reached during the stages of slab rollback
 454 (Fig. 6e), during which the trench velocity peaks. The sub-plate mantle reaches viscos-
 455 ity values on the order of 10^{21} Pa s, approximately one order of magnitude higher than
 456 during SP-velocity peaks.

457 From 50 My, a third slab-folding episode occurs, but with a smaller amplitude due
 458 to the obliquity of slab relative to the viscosity jump (Fig. 6f), and a smaller increase
 459 in v_{sp} . Overall, through time, all velocities decrease and tend towards 1 cm/yr, compa-
 460 rable to the sinking velocity of the deepest part of the slab within the lower mantle. Slab
 461 sinking rates in the lower mantle therefore strongly modulate, and perhaps even limit,
 462 surface kinematics.

463 The kinematic ratio, K_r , given in Equation 1 provides an alternative quantitative
 464 diagnostic. During the free-sinking stage, the slab-tip velocity reaches a peak value of
 465 20 cm/yr, higher than the peak SP velocity v_{sp} (13 cm/yr). As a consequence, the kine-
 466 matic ratio $K_r \leq 1$ (Fig. 6g). After the slab has interacted with the 660-km disconti-
 467 nuity K_r display oscillations. These oscillation follow those observed for v_{sp} and v_t , when
 468 one of the two increases while the other decreases. Folding episodes occur when $K_r >$

469 1, while slab-retreating stages occurs for lower $K_r \simeq 1$. Through time, the amplitude
 470 of K_r oscillations decrease, reflecting the decrease in folding as the slab inclines and the
 471 impact angle with the 660-km viscosity discontinuity decreases.

472 *4.1.2 Slab morphologies and kinematic ratios across all standard cases*

473 We run a series of standard simulations with various initial plate ages (20-100 for
 474 the overriding plate; 10-100 for the subducting plate). Since we focus on the long-term
 475 evolution of these systems (i.e. well after the first stage of slab-free sinking through the
 476 upper mantle), Figure 7a only displays their state at $t = 80$ My.

477 Several studies have focused on the interaction and passage of slabs through the
 478 mantle transition and the resulting slab morphologies (Torii & Yoshioka, 2007; Billen,
 479 2010; Lee & King, 2011; Čížková & Bina, 2013; Billen & Arredondo, 2018), sometimes
 480 characterizing a range of so-called subduction regimes (Garel et al., 2014; Agrusta et al.,
 481 2017; Z.-H. Li et al., 2019; Briaud et al., 2020). Here we focus on two features after ini-
 482 tial slab-660 interaction: trench motion and the amount of slab folding. Thus we define
 483 three regimes: strong trench retreat without slab folding (SR), strong trench retreat with
 484 slab folding (SRwF), and a weak trench retreat with slab folding (WRwF) (7a). The strong-
 485 retreat modes are those for which the total displacement of the trench during the sim-
 486 ulation amounts to an average rate higher than 1 cm/yr, and weak-retreat modes when
 487 it is ≤ 1 cm/yr. Following, Garel et al. (2014), the results of simulations are reported
 488 as functions of initial SP and OP ages, with the former controlling slab buoyancy and
 489 resistance to bending, and the latter controlling the OP bending resistance opposing trench
 490 retreat. Note that due to our focus on the long-term trench motion and the tendency
 491 and nature of slab folding, the subduction regimes outlined herein differ from those used
 492 in Garel et al. (2014).

493 The SR regime in the simulations of the standard case occurs for both relatively
 494 old SPs and relatively old OPs. The regime WRwF occurs only for very young SPs. The
 495 regime that lies in between, SRwF, occurs over the widest parameter space. In simula-
 496 tions with relatively young OPs, only the SRwF is observed. For extremely young cases
 497 ($A_{SP} = A_{OP} = 20$ Myr), subduction is rapidly terminated through slab detachment,
 498 because the low slab pull cannot initially overcome the resisting forces.

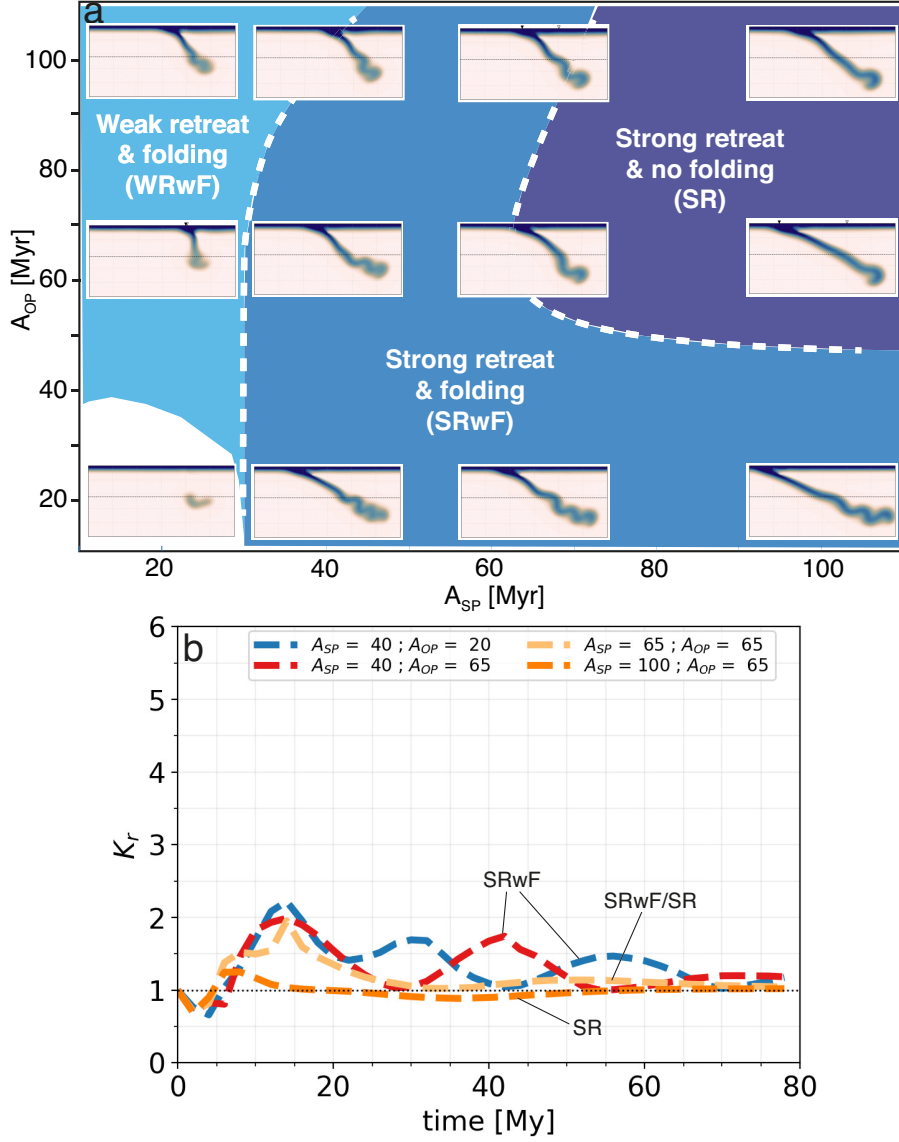


Figure 7. a) Snapshots of the final state (after model run times of 80 My) of all standard models superimposed on a regime diagram. The three regimes are: strong trench retreat without slab folding (SR, purple), strong trench retreat with slab folding (SRwF, dark blue), and weak trench retreat with slab folding (WRwF, light blue). The boundaries between regimes are approximate. b) Kinematic ratio K_r as a function of the time since the initiation of subduction, for four of the standard models shown in (a). The subduction regimes associated with the evolution of those models is indicated by labels. Over time, all four models tend towards no-folding ($K_r \approx 1$).

499 Figure 7b displays the evolution of K_r for four selected standard simulations. These
 500 simulations display peak K_r of 1.5-2.2, shortly after the first slab-660 interaction (time
 501 range 5 to 20 Myr). Simulations [$A_{sp}=40$ My ; $A_{op}=20$ My] (ref. simulation - SRwF)
 502 and [$A_{sp}=40$ My ; $A_{op}=65$ My] (SRwF) display oscillations of K_r associated with slab
 503 folding. Simulations [$A_{sp}=65$ My ; $A_{op}=65$ My] (SR) and [$A_{sp}=100$ My ; $A_{op}=65$ My]
 504 (SR) display $K_r \sim 1$ at all times after initial slab-660 interaction. At later times, the
 505 value of K_r tends to 1, associated a decrease of both v_{sp} and v_s (see Fig. S9 of Supp.
 506 Inf.).

507 4.2 WAL cases

508 We next perform simulations with a WAL, that is simulations where we impose val-
 509 ues of the weakening factor $\alpha < 1$ in the sub-lithospheric mantle. We first consider the
 510 a WAL case of moderate weakening of the sub-plate mantle by a factor of two ($\alpha = 0.5$),
 511 followed by a more extreme scenario of weakening by a factor of 5 (pronounced WAL case
 512 – $\alpha = 0.2$).

513 4.2.1 Reference simulation of the WAL case

514 The plate ages are chosen identical to the reference standard case: $A_{sp}=40$ My and $A_{op}=20$ My.
 515 We apply a two-fold weakening factor ($\alpha = 0.5$). In this simulation reference simula-
 516 tion of the WAL case (Fig. 8), the first slab-660 interaction occurs at ~ 1.5 My, earlier
 517 than in the comparable standard simulation ($\simeq 4$ My). The first slab buckling episode
 518 occurs shortly after, at 2-10 My (Fig. 8a-b), with subducting plate and trench velocities
 519 of 5.5 cm/yr and 1 cm/yr, respectively. Compared to the reference standard simulation,
 520 the velocities are higher in the WAL simulation during these stages, which likely enhances
 521 the strain rate in the sub-plate mantle where the WAL lies. In addition to this intrin-
 522 sic weakening effect, the lowering of the viscosity by a factor of 0.5 leads to WAL vis-
 523 cosities that can be as low as 10^{19} Pa s even after the first slab-660 interaction.

524 A second folding episode takes place after 10 My (Fig. 8c-d) during which the SP
 525 velocity increases from 1.8 to 3.8 cm/yr between $t = 14$ My and $t = 22$ My and that
 526 of the trench decreases from 1.8 to 0.8 cm/yr. The next folding episode (between $t =$
 527 35 My and $t = 55$ My, Fig. 8e) is associated with a stationary trench, while the SP ve-
 528 locity stabilizes at ~ 2.5 cm/yr. A third fold forms after $t = 55$ My (Fig. 8f), which

529 produces a peak subducting-plate velocity of 4.8 cm/yr. The lowest viscosity of the sub-
 530 plate mantle is between 10^{19} and 5×10^{19} Pa s at various stages of the WAL simula-
 531 tion. It never exceeds 10^{20} Pa s, even during stage of slab rollback when SP velocity is
 532 typically low (see Supplementary Text S4 and Figure S10 in the Supplementary Info.).

533 The opposite evolution of trench and SP velocity, associated with K_r oscillation,
 534 is even more apparent in the reference WAL simulation than in the reference simulation
 535 of the standard case. Since the slab tip velocity remains nearly constant at around 1 cm/yr,
 536 independent of slab folding and oscillation of surface velocities, the peaks of K_r in the
 537 WAL simulation are due to the peaks in SP velocity which occur simultaneously of the
 538 lows in trench motion.

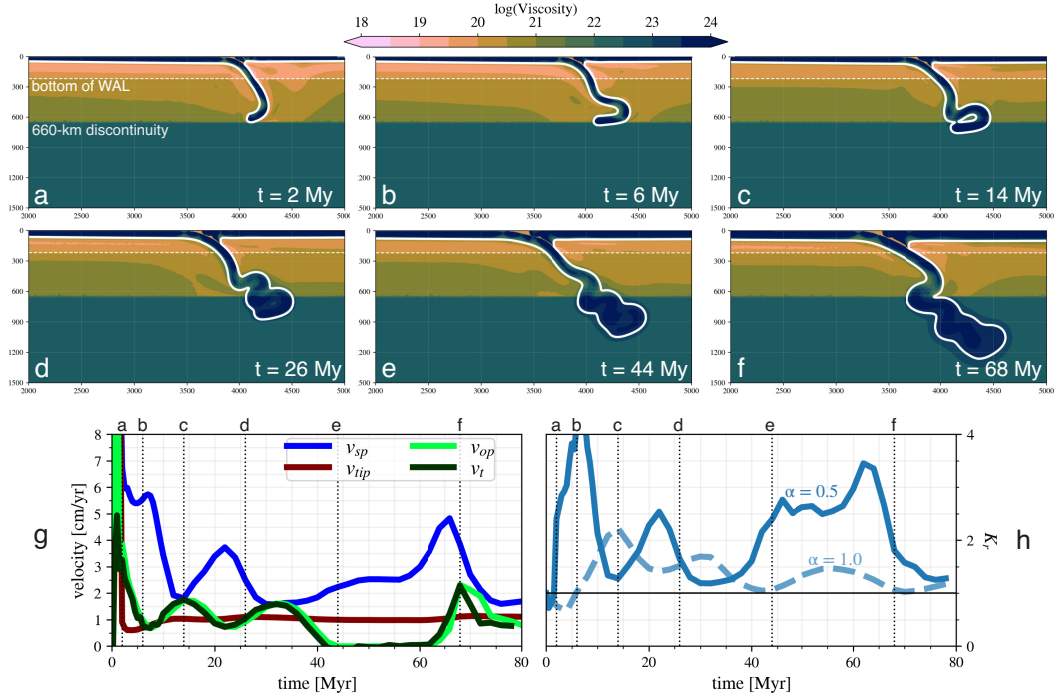


Figure 8. Reference simulation [$A_{sp}=40$ Myr ; $A_{op}=20$ Myr] of the WAL case with a two-fold viscosity reduction ($\alpha = 0.5$). Panels and plotting styles as in Fig. 6. Panel (h) displays the evolution of K_r for this reference WAL case (solid blue) and also for the reference standard case of Fig. 6 (dashed blue).

539

4.2.2 Mantle drag forces on the subducting plate

540

541

542

543

544

545

546

547

548

549

550

551

552

At simulation start, the age of the subducting plate at the trench is 40 My in both the reference standard and the reference WAL models. Hence both models feature identical slab pull initially. At simulation end ($t = 80$ My), the SP is 105km thick at the trench (1100°C-isotherm) for the reference WAL case, versus 110km for the reference standard case. Hence the differences in slab pull force in the upper mantle are likely minor in the two simulations. The mid-ocean ridge is free to move over time, and it migrates trenchward by hundreds of kilometers over 80 My runtime, in both models (see Figures S3 and S5). Since the thicknesses and dimensions of the subducting plate remain quite similar in both model cases, the differences in “ridge push force” (driven by potential energy of ridge topography) should be too small to make an appreciable difference in driving plate velocities. Besides, the magnitude of the ridge-push force is estimated about one order of magnitude smaller than that of the slab-pull force (e.g., Forsyth & Uyeda, 1975; Parsons & Richter, 1980; Turcotte & Schubert, 2002).

553

554

555

556

557

Hence the divergent evolution of the two reference simulations is most likely explained by a reduction of mantle drag at the base of the subducting plate. We calculate the drag force as the integral of the tangential stress along the 1100°C isotherm (in N m^{-1}). Figure 9 displays the temporal evolution of this diagnostic for the reference simulations (with and without a WAL).

558

559

560

561

562

563

564

Prior to first slab-660 interaction, both models show sub-lithospheric mantle moving towards the trench, but with velocities reduced relative to the overlying lithosphere (Couette-type flow). Shear stresses beneath the SP are positive and those beneath the OP are mostly negative. Shear stresses along the base of the SP remains positive after slab-660 interaction (Fig. 9c,e), and the drag force remains negative. The absolute value of the drag force beneath the SP decreases with time, as a consequence of the reduction in length of that plate with time.

565

566

567

568

569

570

The two simulations display similar oscillatory trends in SP velocity, which reflect slab folding behavior. The lower absolute drag in the WAL simulation explains its higher SP velocities (Fig. 8g) relative to the comparable non-WAL case (Fig. 6g). A faster SP may hamper trench retreat via faster trench-ward asthenospheric flow, which would oppose to slab rollback (Alsaif et al., 2020). Alternatively, A. F. Holt and Becker (2016) proposed that a reduction in the sub-plate mantle viscosity would decrease the mantle

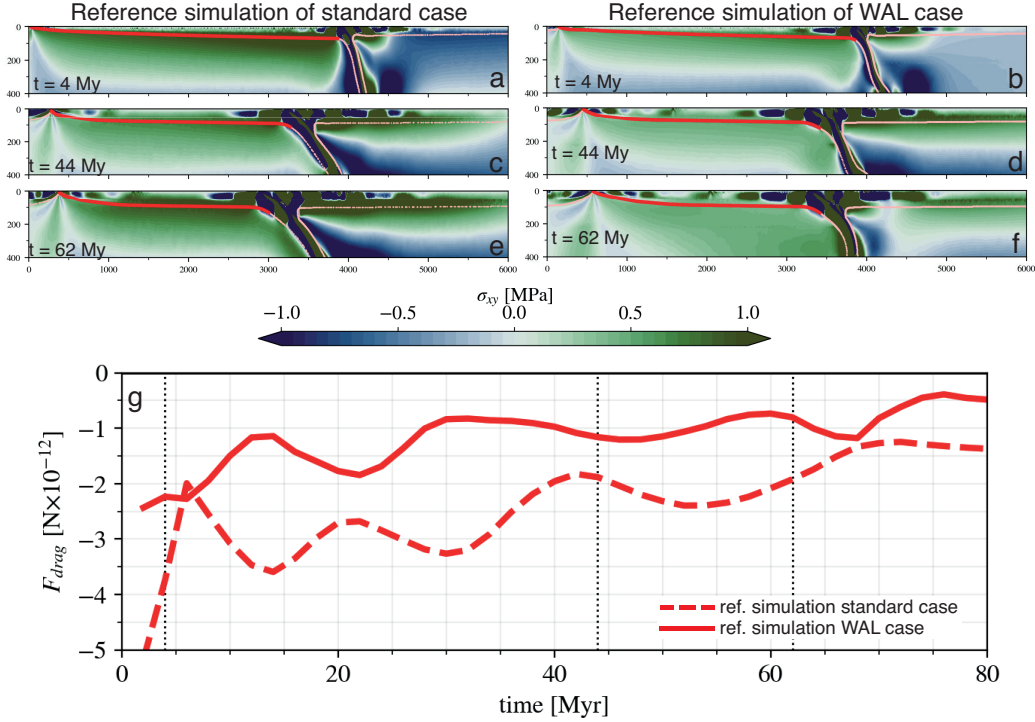


Figure 9. Viscous mantle resistance acting below the subducting plate in the reference standard model versus in the reference WAL model. (a,c,e) Snapshots of the shear stress field (background colour) in the reference standard model at times 4 Myr, 44 Myr, and 62 Myr. (b,d,f) Same snapshots for the reference WAL model. Red line traces the LAB isotherm of 1100°C used to calculate the drag below the subducting plate. Positive shear stresses imply that the tangential component of the stress vector - calculated along the quasi-horizontal LAB isotherm of the subducting plate - is toward the left. g) Evolution of the mantle drag force below the subducting plate for the reference standard model (dashed red) and the reference WAL model (solid red). Negative values denote a force toward the left. The total mantle drag force onto the subducting plate is negative in accordance with the stress vector. Three vertical dashed lines indicate the times of the snapshots (a-f). The drag force beneath the overriding plate is less straightforward to analyze, see Supplementary Information Text S5.

571 drag force acting on the SP to a greater extent than it would decrease the mantle-wedge
 572 suction force (Tovish et al., 1978) which opposes to trench motion. As a consequence,
 573 these authors suggested that a reduction in sub-plate mantle viscosity would preferen-
 574 tially favor a decrease in trench motion. Finally, a lower drag of the asthenosphere on
 575 the subducting slab can also be promoted through the non-newtonian viscosity associ-

576 ated to dislocation creep, causing a positive feedback loop with faster slab inducing larger
 577 strain rate and lower viscous resistance to sinking (Garel et al., 2020). All these effects
 578 favor the higher K_r observed in the reference WAL case compared to the reference stan-
 579 dard case.

580 We ran a modified reference WAL simulation where the WAL is imposed only be-
 581 neath the subducting plate (“WAL-SP” model shown in Fig. S12). Its trench displace-
 582 ment and slab morphology are intermediate between the reference WAL and reference
 583 standard cases, though tending to a WRwF regime and thus closer overall to the WAL
 584 case. This also points to viscosity reduction beneath the SP as the major, causal mech-
 585 anism for shifting subduction towards a WRwF regime when a WAL is imposed.

586 *4.2.3 Subducting slab morphologies and kinematic ratios in the mod-* 587 *erate WAL case ($\alpha = 0.5$)*

588 As with the standard cases, we run a series of WAL simulations with $\alpha = 0.5$, span-
 589 ning plate ages from 20-100 My. Figure 10a displays their final state at 80 My, together
 590 with the inferred regime diagram. Consistent with the standard cases, WAL cases ex-
 591 hibit three regimes (SR, SRwF, and WRwF), but regime boundaries are shifted towards
 592 higher plate ages. In particular, the WAL simulations [$A_{sp}=65$ My- $A_{op}=65$ My] and [$A_{sp}=65$ My-
 593 $A_{op}=100$ My] now lie more clearly in the SRwF regime while their standard equivalents
 594 belong to the SR regime. Moreover, the WAL simulations with $A_{sp} = 40$ My lie within,
 595 or very close to, the WRwF regime, whereas for standard cases, only those with $A_{sp} \geq$
 596 20 My are within this regime.

597 Figure 10b displays the kinematic ratio K_r of selected WAL simulations. As in the
 598 standard cases, the ratios K_r before and during the first slab-660 interaction is gener-
 599 ally higher than 1. Some peak values of K_r reached in the WAL simulations are even
 600 greater (> 2) than the highest values observed in the standard simulations (7b). Most
 601 importantly, two of these simulations [$A_{sp} = 40$ My; $A_{op} = 20$ My] (ref. simulation
 602 for the WAL case) and [$A_{sp} = 65$ My; $A_{op} = 65$ My] display $K_r > 2$ even after the
 603 first slab-660 interaction: the presence of a weak layer favors the excess accumulation
 604 of subducted material in the mantle relative to the accommodation by motion of both
 605 the trench and slab tip, resulting in substantial slab folding. The simulation [$A_{sp}=100$ My ; $A_{op}=65$ My]
 606 shows values of K_r close to 1 at all times after initial slab-660 interaction, consistent with

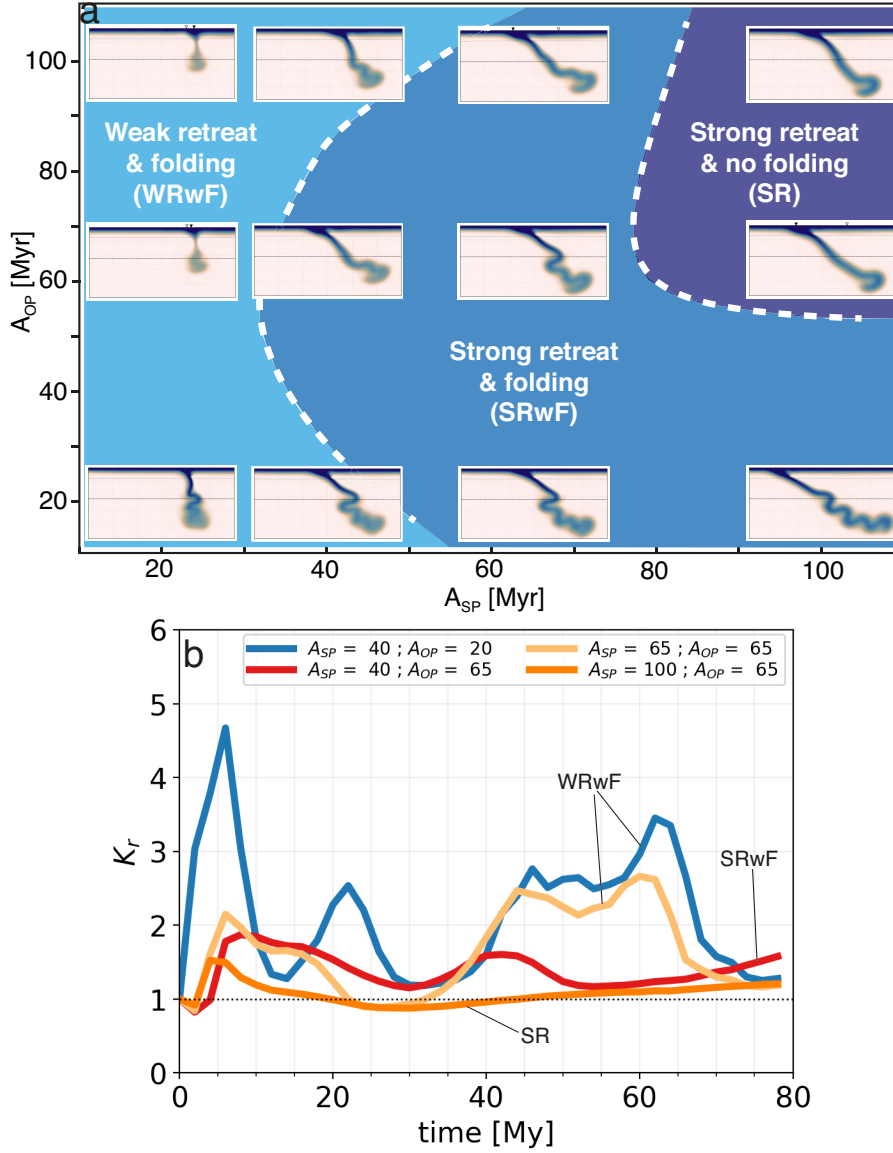


Figure 10. a) Regime diagram of WAL models with two-fold viscosity reduction ($\alpha = 0.5$). Panels and plotting styles as in Fig. 7.

607 the standard case, lying in the SR regime. WAL simulation [$A_{sp}=65$ My ; $A_{op}=65$ My]
 608 exhibits intermediate behavior, with oscillations of K_r up to 1.5, while its standard equiv-
 609 alent show values close to 1. This is because the former clearly lies in the SRwF regime
 610 while its equivalent standard case lies near the transition from the SRwF to the SR regime.

611 **4.2.4 Pronounced WAL cases with $\alpha = 0.2$**

612 We finally run a series of simulations for a five-fold weakened WAL with $\alpha = 0.2$
 613 (Fig. 11a). The most striking difference to all previous cases is that the SR regime (strong
 614 retreat without folding) no longer appears within the range of plate ages investigated,
 615 spanning $A_{sp} = [20 My, 100 My]$ and $A_{op} = [20 My, 100 My]$. Instead, slab folding
 616 becomes pervasive throughout the age parameter space. Moreover, the boundary between
 617 the WRwF and SRwF regimes shifts to subducting plate ages older than 65 My, and over-
 618 riding plate ages older than 20 My. Hence strong trench retreat ($v_t > 1$ cm/yr) now
 619 only occurs for dense and stiff subducting plates, with the WRwF regime (folding un-
 620 der quasi-stationary trenches) becoming dominant. In particular, when the overriding
 621 plate is weak ($A_{op} \simeq 20$ My), ubiquitously folding slabs pile up almost vertically in the
 622 lower mantle. The $\alpha = 0.2$ simulations also sustain higher K_r values (1.5-4) well af-
 623 ter the first slab-600 interaction (Fig. 11b).

624 In most of the pronounced-WAL simulations, soon after the initiation of the model
 625 thermal diffusion (cooling from the surface) prevails over advection, and the ridge on the
 626 OP side disappears. This enforces a quasi-null trench retreat and enhances vertical fold-
 627 ing. As a consequence, the WRwF regime becomes self-sustained from early stages of
 628 these simulations.

629 In most of the pronounced-WAL ($\alpha = 0.2$) simulations, transient thermal insta-
 630 bilities form within the weak layer for simulations with relative old and thick OPs. Drips
 631 of cold lithosphere are generated beneath the OP as the lithosphere thicken by conduc-
 632 tive cooling. The drips are then advected by lateral mantle flow and mix with the un-
 633 derlying mantle. They only occur when WAL viscosity is close to or below $\sim 10^{19}$ Pa s,
 634 consistent with previous studies (van Hunen et al., 2003; Ballmer et al., 2011; Le Voci
 635 et al., 2014; D. R. Davies et al., 2016). Finally, simulations run with $\alpha = 0.1$ (not shown)
 636 exhibit pronounced thermal instabilities beneath both OP and SP, over a wide range of
 637 plate ages (thicknesses). A more detailed analysis of this small-scale convection, how-
 638 ever, out of the scope of this study.

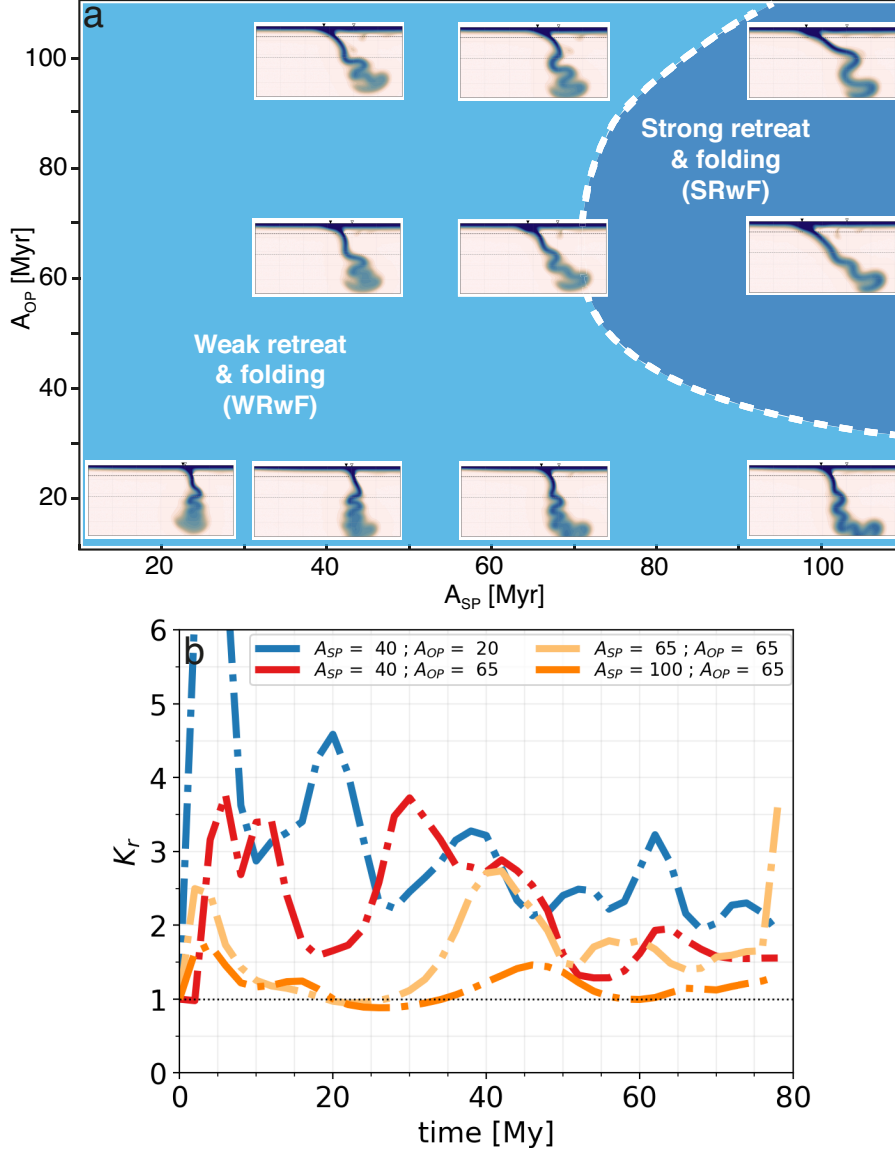


Figure 11. Regime diagram of WAL models with a five-fold viscosity reduction ($\alpha = 0.2$). Panels and plotting styles as in Fig. 7. The models remain in the weak retreat and folding regime over the entire run time, unless they feature very old plate ages.

5 Discussion

5.1 Surface velocities and kinematic ratios

On Earth, subduction rates are typically 3 to 5 times higher than absolute trench velocities, and 5 times higher than estimated slab sinking velocities (see Section 2). This yields kinematic ratio K_r estimates above 1 for most subduction zones, implying that slab thickening/folding is the default regime (see section 2.2).

645 Simulations without a WAL produce surface kinematics at odds with these obser-
 646 vational constraints because once the slab has interacted with the transition zone, the
 647 subducting plate v_{sp} slows down to approach slab sinking rates of 1 cm/yr. The addi-
 648 tion of a WAL renders the simulations more compatible with observational constraints,
 649 in that v_{sp} up to 5 cm/yr are maintained long after initial slab-660 interaction (Fig. S3-
 650 S4 in Supp Info), and trench velocities v_t are attenuated to typically lower than 1 cm/yr.
 651 Our simulations with WAL thus reproduce the rapid subduction rate, near-stationary
 652 trenches, and slow slab-sinking rates observed on Earth. WAL simulations have higher
 653 K_r values than the standard models, as summarized by Figure 12. The time-averaged
 654 kinematic ratio \bar{K}_r (after initial slab-660 interaction, i.e., averaged between 20-80 My)
 655 ranges from 1.0–1.3 in the standard models (Fig. 12a, except for the youngest SP plate
 656 ages). In contrast, \bar{K}_r ranges between 1.0–3.1 in the WAL simulations ($\alpha = 0.5$, Fig. 12b),
 657 and between 1.0–2.9 for the pronounced-WAL simulations ($\alpha = 0.2$, Fig. 12c). \bar{K}_r is
 658 generally higher in the pronounced-WAL simulations (although the maximum value of
 659 $\bar{K}_r = 3.1$ occurs for $\alpha = 0.5$ and the youngest plate ages).

660 Simulations with a WAL also show higher peak values of (non-averaged) K_r , be-
 661 fore and after first slab 660-interaction. In the standard models, K_r mostly ranges be-
 662 tween 1–2 (see Fig. 7 and Supp Info Fig. S9a), whereas the simulations with a WAL ex-
 663 hibit peak K_r values above 2 and up to 6-7 (Figs. 10 and Fig. 11 – see also Figs. S9b,c
 664 in Supp. Info.). Hence only the models with a WAL produce kinematic ratios K_r that
 665 are comparable to those estimated for subduction zones in nature (Fig. 4).

666 Behr and Becker (2018) have suggested the lubrication effect of a weak sedimen-
 667 tary layer above the subducting plate, which gets wedged against the overriding plate
 668 at the plate interface, as an alternative mechanism for increasing v_{sp} in models of sub-
 669 duction dynamics (see also Duarte et al., 2013). They showed that v_{sp} could increase by
 670 one to two orders of magnitude if sediments reduced viscous resistance at the interface
 671 by a comparable amount. Pokorný et al. (2021) demonstrated these possible feedbacks
 672 in a subduction system where the weak interface layer has a strain-rate dependent rhe-
 673 ology, which may undergo viscosity variations according to the changes in the dynam-
 674 ics of the system. Hence we sought to clarify the role of a weakened plate interface in
 675 our own simulations. First we verified that the viscosity of the subduction interface is
 676 similar in the WAL and in the standard reference models, at all temporal stages (Fig.
 677 S13). This confirms that the very different kinematics of these two models really are due

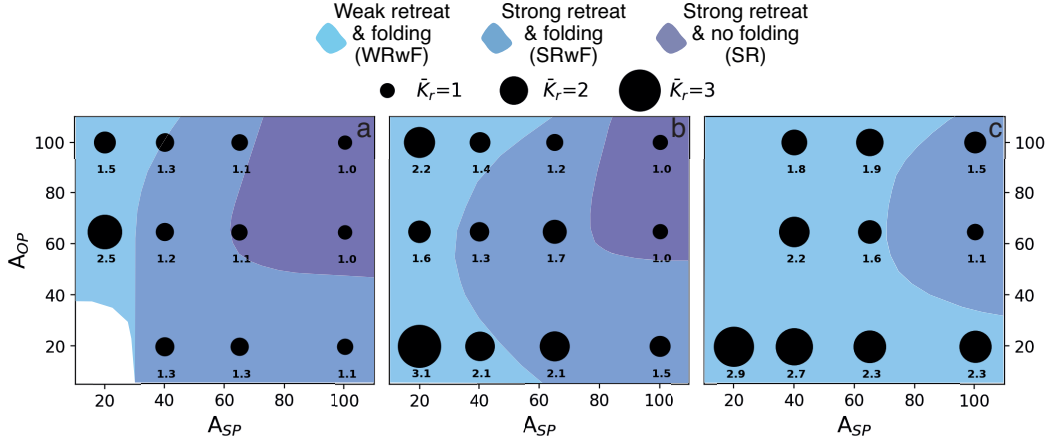


Figure 12. Summary of modeling runs and regime diagrams. Time-averaged kinematic ratio \bar{K}_r after the first slab-600 interaction, plotted in the two-dimensional space of SP and OP plate ages (unit Myr). for (a) standard non-WAL simulations; (b) WAL simulations with $\alpha = 0.5$; (c) pronounced-WAL simulations with $\alpha = 0.2$. \bar{K}_r is represented by black dots with sizes proportional to \bar{K}_r values, which are also printed. Background colors denote folding regimes as in previous figures. The time-averaging window for obtaining \bar{K}_r is [20-80] My.

678 to the lubrication effect by the WAL, rather than an indirect effect of weaker interface
 679 coupling in one model but not the other. Moreover, recent models have shown that a weaker
 680 plate interface tends to produce increased trench retreat v_t (Pusok et al., PREPRINT;
 681 Behr et al., 2022). We attempted to reproduce this finding by running a standard sim-
 682 ulation featuring a plate interface layer with a two-fold reduction in maximum viscos-
 683 ity (see Fig. S8). Relative to the equivalent standard case, v_t did indeed increase slightly,
 684 and so did v_{sp} . In combination, K_r hardly changed compared to the standard model,
 685 thus remaining too low compared to observations. Hence a weaker plate interface does
 686 not narrow the gap between standard model predictions and the available observational
 687 constraints and is thus not considered a valid alternative to the WAL hypothesis.

688 5.2 Slab morphologies

689 The presence of a WAL strongly impacts the subduction regimes and lower man-
 690 tle slab morphologies, as encapsulated by the proxy of K_r . Simulations without a WAL
 691 produce low-to-moderate values of K_r , and moderate-to-high trench retreat rates. With-
 692 out a WAL, strong-retreat regimes are thus dominant across the parameter space exam-

693 ined, and only models with the youngest, weakest overriding plate (20 My) exhibit some
 694 slab-folding behaviour. In the simulation with a WAL and a weakening factor $\alpha = 0.2$,
 695 the (non-folding) SR regime disappears and the SRwF regime only occurs in simulations
 696 with relatively stiff and buoyant plates ($A_{sp} > 80$ My, $A_{sp} > 40$ My). Hence, folding
 697 slabs and vertically piling in the lower mantle, beneath near-stationary trenches, become
 698 the prevailing morphologies when accounting for a WAL in the simulations (light blue
 699 shading in Fig.12). These results demonstrate, for the first time, that models of subduc-
 700 tion dynamics (without external forcing) are able to produce lower-mantle slab morpholo-
 701 gies observed by tomography, while also honouring the plate and trench velocities mea-
 702 sured at the surface.

703 We note that the amplitude of lower-mantle slab folds in our simulations is con-
 704 sistent with theoretical predictions based on a thin-sheet mathematical formulation. Ribe
 705 (2003) and Ribe et al. (2007) used these formulations to derive a scaling law for the am-
 706 plitude of folds of a vertically descending, viscous sheet that buckles as it encounters re-
 707 sistance at a sharp viscosity jump, or a rigid barrier. The predicted fold amplitude is half
 708 the fall height, which would be half the thickness of the upper mantle in the context of
 709 subduction: approximately 330 km. Our simulations with more pronounced vertical slab
 710 folding produce 300 to 500-km wide folds in the lower mantle, that are consistent with
 711 this theory. We note that the presence of a WAL enhances the frequency of folding in
 712 the models but leaves their width reasonably unchanged. The modeled fold amplitudes
 713 of 300-500 km are moderately smaller than the 400-700 km wide “slab walls” imaged by
 714 seismic tomography (e. g. Sigloch & Mihalynuk, 2013). It remains to be investigated whether
 715 this difference is due to shortcomings of the physical approximations used in our dynamic
 716 models, or due to tomographic blur.

717 From models of subduction dynamics, it has been suggested that sustained, quasi-
 718 periodic slab folding, over tens of millions of years after initial slab-660 interaction, can
 719 occur only if the mineralogical phase transition around 410 and 660 km were included
 720 in the models (Béhounková & Čížková, 2008; Čížková & Bina, 2013; Agrusta et al., 2017;
 721 Briaud et al., 2020), and/or if the subducting slab was quite weak, e.g., made of young
 722 seafloor (Garel et al., 2014; Agrusta et al., 2017; Strak & Schellart, 2021). While we ac-
 723 knowledge that these factors may further enhance slab folding, we stress that our sim-
 724 ulations with a WAL did not require the phase transitions in order to produce sustained
 725 slab folding. The Clapeyron slopes of the phase transitions remain under discussion (see

e.g. Agrusta et al., 2017, and references therein), so their relative role in slab folding remains to be clarified. In a similar vein, the inclusion of a WAL yielded slab folding of relatively thick and stiff subducting plates (Fig.12). No additional slab-weakening mechanism or slab-buoyancy variation was required. We note that it has also been suggested that vertical piles of lower-mantle slabs are more easily produced in the context of a fixed overriding plate (Lee & King, 2011; Běhouňková & Čížková, 2008; Čížková & Bina, 2013; Billen & Arredondo, 2018). Here we have demonstrated that vertical slab folding slab can also occur in simulations with a WAL, in which trench retreat remains self-consistently limited (Fig. 8).

6 Conclusion

Previous numerical and analogue models of subduction dynamics tend to produce surface kinematics and lower-mantle slab morphologies that do not match first-order observational constraints. We have shown that including a weak asthenospheric layer below the lithosphere into numerical models of subduction dynamics eliminates these mismatches. The lubricating effect of the asthenosphere produces a velocity increase of the subducting plate and a reduction of trench retreat, yielding predicted velocities that closely match those recorded on Earth. These velocity changes are sustained long after the subducting slab has penetrated into the lower mantle. The surplus of rapidly subducting lithosphere is accommodated by folding, rather than by accelerating trench retreat or slab sinking. This leads to an apparent horizontal widening of the slab in the lower mantle, as is observed by seismic tomography. Substantial near-vertical slab piles accumulate over time because trench motion is limited. We find that a viscosity reduction below the plate by a factor of only 2 to 5 is sufficient to completely shift the dynamics in these models – from non-folding with slow subduction and substantial trench retreat, to regimes of multiply folded, wall-like slab piles under near-stationary trenches. The latter then dominate across a wide parameter space of subducting and overriding plate ages. Our results provide strong independent support for the presence of a weak asthenospheric layer beneath Earth’s lithosphere.

7 Open Research

The data used for Figure 1 and for the estimates of K_r in Fig. 4 is provided in the Supplementary Information Table S1, and is available through the ‘SubMAP’ website

757 <http://submap.gm.univ-montp2.fr/>. The tomography model DETOX-P2 used in Fig.
 758 4 is freely available through the ‘SubMachine’ tomography web portal: <http://submachine.earth.ox.ac.uk/>.
 759 The numerical code, Fluidity, used for the 2-D simulations is open source and available
 760 from <https://fluidityproject.github.io/>. The input files required to reproduce all simu-
 761 lations have been made available in the Zenodo repository <https://doi.org/10.5281/zenodo.6817177>
 762 which also contains the output files of the reference simulations of both the standard and
 763 the WAL cases.

764 Acknowledgments

765 N. C. and K.S. were supported by funding to K.S. from the European Research Coun-
 766 cil (ERC) under the European Union’s Horizon 2020 research and innovation program
 767 (grant agreement 639003 DEEP TIME). This work was supported by the French gov-
 768 ernment, through the UCAJEDI Investments in the Future project managed by the Na-
 769 tional Research Agency (ANR) under reference number ANR-15-IDEX-01. The authors
 770 are grateful to the OPAL infrastructure from Université Côte d’Azur and the Univer-
 771 sité Côte d’Azur’s Center for High-Performance Computing for providing resources and
 772 support.

773 References

- 774 Agrusta, R., Goes, S., & van Hunen, J. (2017). Subducting-slab transition-zone
 775 interaction: Stagnation, penetration and mode switches. *Earth and Planetary
 776 Science Letters*, *464*, 10–23. Retrieved from [https://doi.org/10.1016/
 777 j.epsl.2017.02.005](https://doi.org/10.1016/j.epsl.2017.02.005) doi: 10.1016/j.epsl.2017.02.005
- 778 Alsaif, M., Garel, F., Gueydan, F., & Davies, D. R. (2020). Upper plate deformation
 779 and trench retreat modulated by subduction-driven shallow asthenospheric
 780 flows. *Earth and Planetary Science Letters*, *532*, 116013.
- 781 Amaru, M. (2007). *Global travel time tomography with 3-d reference models*
 782 (Vol. 274). Utrecht University.
- 783 Arcay, D., Lallemand, S., & Doin, M.-P. (2008). Back-arc strain in subduction zones:
 784 Statistical observations versus numerical modeling. *Geochemistry, Geophysics,
 785 Geosystems*, *9*(5).
- 786 Argus, D. F., Gordon, R. G., & DeMets, C. (2011). Geologically current motion
 787 of 56 plates relative to the no-net-rotation reference frame. *Geochemistry,*

- 788 *Geophysics, Geosystems*, 12(11). Retrieved from [https://doi.org/10.1029/](https://doi.org/10.1029/2011GC003751)
789 2011GC003751 doi: 10.1029/2011GC003751
- 790 Arredondo, K. M., & Billen, M. I. (2017). Coupled effects of phase transitions and
791 rheology in 2-d dynamical models of subduction. *Journal of Geophysical Re-*
792 *search: Solid Earth*, 122(7), 5813–5830. Retrieved from [https://doi.org/10](https://doi.org/10.1002/2017JB014374)
793 .1002/2017JB014374 doi: 10.1002/2017JB014374
- 794 Ballmer, M. D., Ito, G., Van Hunen, J., & Tackley, P. J. (2011). Spatial and tempo-
795 ral variability in hawaiian hotspot volcanism induced by small-scale convection.
796 *Nature Geoscience*, 4(7), 457–460.
- 797 Barruol, G., Sigloch, K., Scholz, J.-R., Mazzullo, A., Stutzmann, E., Montag-
798 ner, J.-P., ... others (2019). Large-scale flow of indian ocean astheno-
799 sphere driven by réunion plume. *Nature Geoscience*, 12(12), 1043–1049.
800 Retrieved from <https://doi.org/10.1038/s41561-019-0479-3> doi:
801 10.1038/s41561-019-0479-3
- 802 Becker, T. W. (2017). Superweak asthenosphere in light of upper mantle seis-
803 mic anisotropy. *Geochemistry, Geophysics, Geosystems*, 18(5), 1986–
804 2003. Retrieved from <https://doi.org/10.1002/2017GC006886> doi:
805 10.1002/2017GC006886
- 806 Becker, T. W., & Faccenna, C. (2009). A review of the role of subduction dynamics
807 for regional and global plate motions. In *Subduction zone geodynamics* (pp. 3–
808 34). Springer.
- 809 Becker, T. W., Schaeffer, A. J., Lebedev, S., & Conrad, C. P. (2015). Toward a
810 generalized plate motion reference frame. *Geophysical Research Letters*, 42(9),
811 3188–3196. Retrieved from <https://doi.org/10.1002/2015GL063695> doi: 10
812 .1002/2015GL063695
- 813 Běhouňková, M., & Čížková, H. (2008). Long-wavelength character of subducted
814 slabs in the lower mantle. *Earth and Planetary Science Letters*, 275(1-2), 43–
815 53. Retrieved from <https://doi.org/10.1016/j.epsl.2008.07.059> doi: 10
816 .1016/j.epsl.2008.07.059
- 817 Behr, W. M., & Becker, T. W. (2018). Sediment control on subduction plate speeds.
818 *Earth and Planetary Science Letters*, 502, 166–173. Retrieved from [https://](https://doi.org/10.1016/j.epsl.2018.08.057)
819 doi.org/10.1016/j.epsl.2018.08.057 doi: 10.1016/j.epsl.2018.08.057
- 820 Behr, W. M., Holt, A. F., Becker, T. W., & Faccenna, C. (2022). The effects of plate

- 821 interface rheology on subduction kinematics and dynamics. *Geophysical Jour-*
 822 *nal International*. Retrieved from <https://doi.org/10.1093/gji/ggac075>
 823 doi: 10.1093/gji/ggac075
- 824 Billen, M. I. (2010). Slab dynamics in the transition zone. *Physics of the Earth*
 825 *and planetary interiors*, 183(1-2), 296–308. Retrieved from [https://doi.org/](https://doi.org/10.1016/j.pepi.2010.05.005)
 826 [10.1016/j.pepi.2010.05.005](https://doi.org/10.1016/j.pepi.2010.05.005) doi: 10.1016/j.pepi.2010.05.005
- 827 Billen, M. I., & Arredondo, K. M. (2018). Decoupling of plate-asthenosphere
 828 motion caused by non-linear viscosity during slab folding in the transi-
 829 tion zone. *Physics of the Earth and Planetary Interiors*, 281, 17–30. Re-
 830 trieved from <https://doi.org/10.1016/j.pepi.2018.04.011> doi:
 831 [10.1016/j.pepi.2018.04.011](https://doi.org/10.1016/j.pepi.2018.04.011)
- 832 Briaud, A., Agrusta, R., Faccenna, C., Funicello, F., & van Hunen, J. (2020).
 833 Topographic fingerprint of deep mantle subduction. *Journal of Geo-*
 834 *physical Research: Solid Earth*, 125(1), e2019JB017962. Retrieved from
 835 <https://doi.org/10.1029/2019JB017962> doi: 10.1029/2019JB017962
- 836 Butterworth, N., Talsma, A., Müller, R., Seton, M., Bunge, H.-P., Schuberth, B.,
 837 ... Heine, C. (2014). Geological, tomographic, kinematic and geodynamic
 838 constraints on the dynamics of sinking slabs. *Journal of Geodynamics*, 73,
 839 1–13. Retrieved from <https://doi.org/10.1016/j.jog.2013.10.006> doi:
 840 [10.1016/j.jog.2013.10.006](https://doi.org/10.1016/j.jog.2013.10.006)
- 841 Čadež, O., & Fleitout, L. (1999). A global geoid model with imposed plate velocities
 842 and partial layering. *Journal of Geophysical Research: Solid Earth*, 104(B12),
 843 29055–29075. Retrieved from <https://doi.org/10.1029/1999JB900150> doi:
 844 [10.1029/1999JB900150](https://doi.org/10.1029/1999JB900150)
- 845 Capitanio, F., Morra, G., & Goes, S. (2007). Dynamic models of downgoing
 846 plate-buoyancy driven subduction: Subduction motions and energy dis-
 847 sipation. *Earth and Planetary Science Letters*, 262(1), 284–297. doi:
 848 [10.1016/j.epsl.2007.07.039](https://doi.org/10.1016/j.epsl.2007.07.039)
- 849 Carluccio, R., Kaus, B., Capitanio, F. A., & Moresi, L. (2019). The impact of a
 850 very weak and thin upper asthenosphere on subduction motions. *Geophysical*
 851 *Research Letters*, 46(21), 11893–11905. Retrieved from [https://doi.org/10](https://doi.org/10.1029/2019GL085212)
 852 [.1029/2019GL085212](https://doi.org/10.1029/2019GL085212) doi: 10.1029/2019GL085212
- 853 Cerpa, N. G., Araya, R., Gerbault, M., & Hassani, R. (2015). Relationship between

- 854 slab dip and topography segmentation in an oblique subduction zone: Insights
855 from numerical modeling. *Geophysical Research Letters*, 42(14), 5786–5795.
856 doi: 10.1002/2015GL064047
- 857 Cerpa, N. G., Guillaume, B., & Martinod, J. (2018). The interplay between over-
858 riding plate kinematics, slab dip and tectonics. *Geophysical Journal Interna-
859 tional*, 215(3), 1789–1802. doi: 10.1093/gji/ggy365
- 860 Cerpa, N. G., Hassani, R., Gerbault, M., & Prévost, J.-H. (2014). A fictitious do-
861 main method for lithosphere-asthenosphere interaction: Application to periodic
862 slab folding in the upper mantle. *Geochemistry, Geophysics, Geosystems*,
863 15(5), 1852–1877. Retrieved from <https://doi.org/10.1002/2014GC005241>
864 doi: 10.1002/2014GC005241
- 865 Chantel, J., Manthilake, G., Andraut, D., Novella, D., Yu, T., & Wang, Y. (2016).
866 Experimental evidence supports mantle partial melting in the asthenosphere.
867 *Science advances*, 2(5), e1600246. Retrieved from [https://doi.org/10.1126/
868 sciadv.1600246](https://doi.org/10.1126/sciadv.1600246)
- 869 Christensen, U. R. (1996). The influence of trench migration on slab penetration
870 into the lower mantle. *Earth and Planetary Science Letters*, 140(1), 27–39.
871 doi: 10.1016/0012-821X(96)00023-4
- 872 Čížková, H., & Bina, C. (2013). Effects of mantle and subduction-interface rheolo-
873 gies on slab stagnation and trench rollback. *Earth and Planetary Science Let-
874 ters*, 379, 95–103. doi: 10.1016/j.epsl.2013.08.011
- 875 Čížková, H., & Bina, C. R. (2015). Geodynamics of trench advance: Insights from a
876 philippine-sea-style geometry. *Earth and Planetary Science Letters*, 430, 408–
877 415. Retrieved from <https://doi.org/10.1016/j.epsl.2015.07.004> doi: 10
878 .1016/j.epsl.2015.07.004
- 879 Čížková, H., van den Berg, A. P., Spakman, W., & Matyska, C. (2012). The
880 viscosity of earth’s lower mantle inferred from sinking speed of subducted
881 lithosphere. *Physics of the earth and Planetary Interiors*, 200, 56–62.
882 Retrieved from <https://doi.org/10.1016/j.pepi.2012.02.010> doi:
883 10.1016/j.pepi.2012.02.010
- 884 Coltice, N., Rolf, T., Tackley, P. J., & Labrosse, S. (2012). Dynamic causes of the
885 relation between area and age of the ocean floor. *Science*, 336(6079), 335–338.
886 Retrieved from <https://doi.org/10.1126/science.1219120> doi: 10.1126/

- 887 science.1219120
- 888 Conrad, C. P., & Behn, M. D. (2010). Constraints on lithosphere net rotation
889 and asthenospheric viscosity from global mantle flow models and seismic
890 anisotropy. *Geochemistry, Geophysics, Geosystems*, *11*(5). Retrieved from
891 <https://doi.org/10.1029/2009GC002970> doi: 10.1029/2009GC002970
- 892 Cooper, R., & Kohlstedt, D. (1986). Rheology and structure of olivine-basalt par-
893 tial melts. *Journal of Geophysical Research: Solid Earth*, *91*(B9), 9315–9323.
894 Retrieved from <https://doi.org/10.1029/JB091iB09p09315> doi: 10.1029/
895 JB091iB09p09315
- 896 Davies, D. R., Le Voci, G., Goes, S., Kramer, S. C., & Wilson, C. R. (2016). The
897 mantle wedge’s transient 3-D flow regime and thermal structure. *Geochem.*
898 *Geophys. Geosys.*, *17*, 78-100. doi: 10.1002/2015GC006125
- 899 Davies, D. R., Wilson, C., & Kramer, S. (2011). Fluidity: A fully unstructured
900 anisotropic adaptive mesh computational modeling framework for geody-
901 namics. *Geochemistry, Geophysics, Geosystems*, *12*(6). Retrieved from
902 <https://doi.org/10.1029/2011GC003551> doi: 10.1029/2011GC003551
- 903 Davies, G. (1981). Regional compensation of subducted lithosphere: effects on geoid,
904 gravity and topography from a preliminary model. *Earth and Planetary Sci-*
905 *ence Letters*, *54*(3), 431–441. Retrieved from [https://doi.org/10.1016/0012-](https://doi.org/10.1016/0012-821X(81)90059-5)
906 [821X\(81\)90059-5](https://doi.org/10.1016/0012-821X(81)90059-5) doi: 10.1016/0012-821X(81)90059-5
- 907 Debayle, E., Bodin, T., Durand, S., & Ricard, Y. (2020). Seismic evidence
908 for partial melt below tectonic plates. *Nature*, *586*(7830), 555–559. Re-
909 trieved from <https://doi.org/10.1038/s41586-020-2809-4> doi:
910 10.1038/s41586-020-2809-4
- 911 Debayle, E., & Ricard, Y. (2013). Seismic observations of large-scale deformation at
912 the bottom of fast-moving plates. *Earth and Planetary Science Letters*, *376*,
913 165–177. Retrieved from <https://doi.org/10.1016/j.epsl.2013.06.025>
914 doi: 10.1016/j.epsl.2013.06.025
- 915 Di Giuseppe, E., Van Hunen, J., Funiciello, F., Faccenna, C., & Giardini, D. (2008).
916 Slab stiffness control of trench motion: Insights from numerical models. *Geo-*
917 *chemistry, Geophysics, Geosystems*, *9*(2).
- 918 Doglioni, C., Carminati, E., Cuffaro, M., & Scrocca, D. (2007). Subduction kinemat-
919 ics and dynamic constraints. *Earth-Science Reviews*, *83*(3), 125–175.

- 920 Domeier, M., Doubrovine, P. V., Torsvik, T. H., Spakman, W., & Bull, A. L. (2016).
 921 Global correlation of lower mantle structure and past subduction. *Geophysi-*
 922 *cal Research Letters*, *43*(10), 4945–4953. Retrieved from [https://doi.org/10](https://doi.org/10.1002/2016GL068827)
 923 [.1002/2016GL068827](https://doi.org/10.1002/2016GL068827) doi: 10.1002/2016GL068827
- 924 Doubrovine, P. V., Steinberger, B., & Torsvik, T. H. (2012). Absolute plate
 925 motions in a reference frame defined by moving hot spots in the pacific, at-
 926 lantic, and indian oceans. *Journal of Geophysical Research: Solid Earth*,
 927 *117*(B9). Retrieved from <https://doi.org/10.1029/2011JB009072> doi:
 928 [10.1029/2011JB009072](https://doi.org/10.1029/2011JB009072)
- 929 Duarte, J. C., Schellart, W. P., & Cruden, A. R. (2013). Three-dimensional dy-
 930 namic laboratory models of subduction with an overriding plate and variable
 931 interplate rheology. *Geophysical Journal International*, ggt257.
- 932 Forsyth, D., & Uyeda, S. (1975). On the relative importance of the driving forces of
 933 plate motion. *Geophysical Journal International*, *43*(1), 163–200.
- 934 French, S., Lekic, V., & Romanowicz, B. (2013). Waveform tomography reveals
 935 channeled flow at the base of the oceanic asthenosphere. *Science*, *342*(6155),
 936 227–230. Retrieved from <https://doi.org/10.1126/science.1241514> doi:
 937 [10.1126/science.1241514](https://doi.org/10.1126/science.1241514)
- 938 Fukao, Y., & Obayashi, M. (2013). Subducted slabs stagnant above, penetrating
 939 through, and trapped below the 660 km discontinuity. *Journal of Geophysical*
 940 *Research: Solid Earth*, *118*(11), 5920–5938. doi: 10.1002/2013JB010466
- 941 Fukao, Y., Obayashi, M., Inoue, H., & Nenbai, M. (1992). Subducting slabs stagnant
 942 in the mantle transition zone. *Journal of Geophysical Research: Solid Earth*
 943 *(1978–2012)*, *97*(B4), 4809–4822.
- 944 Funiciello, F., Faccenna, C., & Giardini, D. (2004). Role of lateral mantle flow in the
 945 evolution of subduction systems: insights from laboratory experiments. *Geo-*
 946 *physical Journal International*, *157*(3), 1393–1406. doi: 10.1111/j.1365-246X
 947 [.2004.02313.x](https://doi.org/10.1111/j.1365-246X.2004.02313.x)
- 948 Funiciello, F., Faccenna, C., Heuret, A., Lallemand, S., Di Giuseppe, E., & Becker,
 949 T. (2008). Trench migration, net rotation and slab–mantle coupling. *Earth and*
 950 *Planetary Science Letters*, *271*(1), 233–240. doi: 10.1016/j.epsl.2008.04.006
- 951 Garel, F., Goes, S., Davies, D. R., Davies, J., Kramer, S., & Wilson, C. (2014).
 952 Interaction of subducted slabs with the mantle transition-zone: A regime

- 953 diagram from 2-d thermo-mechanical models with a mobile trench and an
 954 overriding plate. *Geochemistry, Geophysics, Geosystems*. Retrieved from
 955 <https://doi.org/10.1002/2014GC005257> doi: 10.1002/2014GC005257
- 956 Garel, F., Thoraval, C., Tommasi, A., Demouchy, S., & Davies, D. R. (2020). Using
 957 thermo-mechanical models of subduction to constrain effective mantle viscos-
 958 ity. *Earth and Planetary Science Letters*, *539*, 116243.
- 959 Gibert, G., Gerbault, M., Hassani, R., & Tric, E. (2012). Dependency of slab geom-
 960 etry on absolute velocities and conditions for cyclicity: insights from numerical
 961 modelling. *Geophysical Journal International*, *189*(2), 747–760. Retrieved
 962 2013-12-05, from <https://doi.org/10.1111/j.1365-246X.2012.05426.x>
 963 doi: 10.1111/j.1365-246X.2012.05426.x
- 964 Goes, S., Agrusta, R., Van Hunen, J., & Garel, F. (2017). Subduction-transition
 965 zone interaction: A review. *Geosphere*, *13*(3), 644–664. Retrieved from
 966 <https://doi.org/10.1130/GES01476.1> doi: 10.1130/GES01476.1
- 967 Goes, S., Capitanio, F. A., Morra, G., Seton, M., & Giardini, D. (2011). Sig-
 968 natures of downgoing plate-buoyancy driven subduction in cenozoic plate
 969 motions. *Physics of the Earth and Planetary Interiors*, *184*(1), 1–13.
 970 Retrieved from <https://doi.org/10.1016/j.pepi.2010.10.007> doi:
 971 10.1016/j.pepi.2010.10.007
- 972 Guillaume, B., Hertgen, S., Martinod, J., & Cerpa, N. (2018). Slab dip,
 973 surface tectonics: How and when do they change following an accelera-
 974 tion/slow down of the overriding plate? *Tectonophysics*, *726*, 110–120. doi:
 975 10.1016/j.tecto.2018.01.030
- 976 Guillou-Frottier, L., Buttles, J., & Olson, P. (1995). Laboratory experiments on
 977 the structure of subducted lithosphere. *Earth and Planetary Science Letters*,
 978 *133*(1), 19–34.
- 979 Gurnis, M. (1993). Phanerozoic marine inundation of continents driven by dynamic
 980 topography above subducting slabs. *Nature*, *364*(6438), 589–593. Retrieved
 981 from <https://doi.org/10.1038/364589a0> doi: 10.1038/364589a0
- 982 Gurnis, M., & Hager, B. H. (1988). Controls of the structure of subducted slabs.
 983 *Nature*, *335*(6188), 317–321. Retrieved from [https://doi.org/10.1038/](https://doi.org/10.1038/335317a0)
 984 [335317a0](https://doi.org/10.1038/335317a0) doi: 10.1038/335317a0
- 985 Hager, B., & Richards, M. (1989). Long-wavelength variations in earth’s geoid:

- 986 physical models and dynamical implications. *Philosophical Transactions*
 987 *of the Royal Society of London. Series A, Mathematical and Physical Sci-*
 988 *ences*, 328(1599), 309–327. Retrieved from [https://doi.org/10.1098/](https://doi.org/10.1098/rsta.1989.0038)
 989 [rsta.1989.0038](https://doi.org/10.1098/rsta.1989.0038) doi: 10.1098/rsta.1989.0038
- 990 Hager, B. H. (1984). Subducted slabs and the geoid: Constraints on mantle rhe-
 991 ology and flow. *Journal of Geophysical Research: Solid Earth*, 89(B7), 6003–
 992 6015. Retrieved from <https://doi.org/10.1029/JB089iB07p06003> doi: 10
 993 .1029/JB089iB07p06003
- 994 Hertgen, S., Yamato, P., Guillaume, B., Magni, V., Schliffke, N., & van Hunen,
 995 J. (2020). Influence of the thickness of the overriding plate on conver-
 996 gence zone dynamics. *Geochemistry, Geophysics, Geosystems*, 21(2),
 997 e2019GC008678. Retrieved from <https://doi.org/10.1029/2019GC008678>
 998 doi: 10.1029/2019GC008678
- 999 Heuret, A., Funicello, F., Faccenna, C., & Lallemand, S. (2007). Plate kinemat-
 1000 ics, slab shape and back-arc stress: a comparison between laboratory models
 1001 and current subduction zones. *Earth and Planetary Science Letters*, 256(3),
 1002 473–483. doi: 10.1016/j.epsl.2007.02.004
- 1003 Heuret, A., & Lallemand, S. (2005). Plate motions, slab dynamics and back-arc de-
 1004 formation. *Physics of the Earth and Planetary Interiors*, 149(1), 31–51. doi:
 1005 10.1016/j.pepi.2004.08.022
- 1006 Höink, T., Lenardic, A., & Richards, M. (2012). Depth-dependent viscosity and
 1007 mantle stress amplification: implications for the role of the asthenosphere in
 1008 maintaining plate tectonics. *Geophysical Journal International*, 191(1), 30–41.
 1009 Retrieved from <https://doi.org/10.1111/j.1365-246X.2012.05621.x> doi:
 1010 10.1111/j.1365-246X.2012.05621.x
- 1011 Holt, A., Becker, T., & Buffett, B. (2015). Trench migration and overriding plate
 1012 stress in dynamic subduction models. *Geophysical Journal International*,
 1013 201(1), 172–192. Retrieved from <https://doi.org/10.1093/gji/ggv011> doi:
 1014 10.1093/gji/ggv011
- 1015 Holt, A. F., & Becker, T. W. (2016). The effect of a power-law mantle viscosity on
 1016 trench retreat rate. *Geophysical Journal International*, ggw392. Retrieved from
 1017 <https://doi.org/10.1093/gji/ggw392> doi: 10.1093/gji/ggw392
- 1018 Holtzman, B. K. (2016). Questions on the existence, persistence, and me-

- 1019 chanical effects of a very small melt fraction in the asthenosphere. *Geo-*
1020 *chemistry, Geophysics, Geosystems*, 17(2), 470–484. Retrieved from
1021 <https://doi.org/10.1002/2015GC006102> doi: 10.1002/2015GC006102
- 1022 Hosseini, K., Sigloch, K., Tsekhmistrenko, M., Zaheri, A., Nissen-Meyer, T., &
1023 Igel, H. (2020). Global mantle structure from multifrequency tomogra-
1024 phy using p, pp and p-diffracted waves. *Geophysical Journal International*,
1025 220(1), 96–141. Retrieved from <https://doi.org/10.1093/gji/ggz394> doi:
1026 10.1093/gji/ggz394
- 1027 Jarrard, R. D. (1986). Relations among subduction parameters. *Reviews of Geo-*
1028 *physics*, 24(2), 217–284. doi: 10.1029/RG024i002p00217
- 1029 Jones, T., Davies, D., Campbell, I., Wilson, C., & Kramer, S. (2016). Do man-
1030 tle plumes preserve the heterogeneous structure of their deep-mantle source?
1031 *Earth Planet. Sci. Lett.*, 434, 10 - 17. doi: 10.1016/j.epsl.2015.11.016
- 1032 Karason, H., & Van Der Hilst, R. D. (2000). Constraints on mantle convection from
1033 seismic tomography. *The History and Dynamics of Global Plate Motions*, 277–
1034 288.
- 1035 Kawakatsu, H., Kumar, P., Takei, Y., Shinohara, M., Kanazawa, T., Araki, E., &
1036 Suyehiro, K. (2009). Seismic evidence for sharp lithosphere-asthenosphere
1037 boundaries of oceanic plates. *science*, 324(5926), 499–502. Retrieved from
1038 <https://doi.org/10.1126/science.1169499> doi: 10.1126/science.1169499
- 1039 Kohlstedt, D. L., & Zimmerman, M. E. (1996). Rheology of partially molten man-
1040 tle rocks. *Annual Review of Earth and Planetary Sciences*, 24(1), 41–62.
1041 Retrieved from <https://doi.org/10.1146/annurev.earth.24.1.41> doi:
1042 10.1146/annurev.earth.24.1.41
- 1043 Kramer, S., Wilson, C., & Davies, D. R. (2012). An implicit free surface algorithm
1044 for geodynamical simulations. *Physics of the Earth and Planetary Interiors*,
1045 194, 25–37. Retrieved from <https://doi.org/10.1016/j.pepi.2012.01.001>
1046 doi: 10.1016/j.pepi.2012.01.001
- 1047 Kramer, S. C., Davies, D. R., & Wilson, C. R. (2021). Analytical solutions for man-
1048 tle flow in cylindrical and spherical shells. *Geosci. Model Dev.*, 14, 1899–1919.
1049 doi: 10.5194/gmd-14-1899-2021
- 1050 Lallemant, S., Heuret, A., & Boutelier, D. (2005). On the relationships between
1051 slab dip, back-arc stress, upper plate absolute motion, and crustal nature

- 1052 in subduction zones. *Geochemistry, Geophysics, Geosystems*, 6(9). doi:
 1053 10.1029/2005GC000917
- 1054 Lee, C., & King, S. D. (2011). Dynamic buckling of subducting slabs reconciles
 1055 geological and geophysical observations. *Earth and Planetary Science Letters*,
 1056 312(3), 360–370.
- 1057 Lenardic, A., Richards, M., & Busse, F. H. (2006). Depth-dependent rheology and
 1058 the horizontal length scale of mantle convection. *Journal of Geophysical Re-*
 1059 *search: Solid Earth*, 111(B7).
- 1060 Le Voci, G., Davies, D. R., Goes, S., Kramer, S. C., & Wilson, C. R. (2014).
 1061 A systematic 2-D investigation into the mantle wedge’s transient flow
 1062 regime and thermal structure: complexities arising from a hydrated rheol-
 1063 ogy and thermal buoyancy. *Geochem. Geophys. Geosys.*, 15, 28–51. doi:
 1064 10.1002/2013GC005022
- 1065 Li, C., van der Hilst, R. D., Engdahl, E. R., & Burdick, S. (2008). A new global
 1066 model for p wave speed variations in earth’s mantle. *Geochemistry, Geo-*
 1067 *physics, Geosystems*, 9(5).
- 1068 Li, Z.-H., Gerya, T., & Connolly, J. A. (2019). Variability of subducting slab
 1069 morphologies in the mantle transition zone: Insight from petrological-
 1070 thermomechanical modeling. *Earth-Science Reviews*, 196, 102874. Re-
 1071 trieved from <https://doi.org/10.1016/j.earscirev.2019.05.018> doi:
 1072 10.1016/j.earscirev.2019.05.018
- 1073 Loiselet, C., Braun, J., Husson, L., Le Carlier de Veslud, C., Thieulot, C., Yam-
 1074 ato, P., & Grujic, D. (2010). Subducting slabs: Jellyfishes in the earth’s
 1075 mantle. *Geochemistry, Geophysics, Geosystems*, 11(8). Retrieved from
 1076 <https://doi.org/10.1029/2010GC003172> doi: 10.1029/2010GC003172
- 1077 Lyu, T., Zhu, Z., & Wu, B. (2019). Subducting slab morphology and mantle tran-
 1078 sition zone upwelling in double-slab subduction models with inward-dipping
 1079 directions. *Geophysical Journal International*, 218(3), 2089–2105. Retrieved
 1080 from <https://doi.org/10.1093/gji/ggz268> doi: 10.1093/gji/ggz268
- 1081 Meyers, C. D., & Kohlstedt, D. L. (2021). Experimental measurements of
 1082 anisotropic viscosity in naturally sourced dunite with a preexisting cpo.
 1083 *Tectonophysics*, 815, 228949. Retrieved from [https://doi.org/10.1016/](https://doi.org/10.1016/j.tecto.2021.228949)
 1084 [j.tecto.2021.228949](https://doi.org/10.1016/j.tecto.2021.228949) doi: 10.1016/j.tecto.2021.228949

- 1085 Mitrovica, J., & Forte, A. (2004). A new inference of mantle viscosity based upon
 1086 joint inversion of convection and glacial isostatic adjustment data. *Earth and*
 1087 *Planetary Science Letters*, 225(1), 177–189. doi: 10.1016/j.epsl.2004.06.005
- 1088 Mohammadzaheri, A., Sigloch, K., Hosseini, K., & Mihalynuk, M. G. (2021). Sub-
 1089 ducted lithosphere under south america from multi-frequency p-wave tomog-
 1090 raphy. *Journal of Geophysical Research: Solid Earth*, 126, e2020JB020704.
 1091 Retrieved from <https://doi.org/10.1029/2020JB020704> doi: 10.1029/
 1092 2020JB020704
- 1093 Montagner, J.-P., & Tanimoto, T. (1991). Global upper mantle tomography of seis-
 1094 mic velocities and anisotropies. *Journal of Geophysical Research: Solid Earth*,
 1095 96(B12), 20337–20351. Retrieved from <https://doi.org/10.1029/91JB01890>
 1096 doi: 10.1029/91JB01890
- 1097 Naif, S., Key, K., Constable, S., & Evans, R. (2013). Melt-rich channel ob-
 1098 served at the lithosphere–asthenosphere boundary. *Nature*, 495(7441),
 1099 356–359. Retrieved from <https://doi.org/10.1038/nature11939> doi:
 1100 10.1038/nature11939
- 1101 Parsons, B., & Richter, F. (1980). A relation between the driving force and geoid
 1102 anomaly associated with mid-ocean ridges. *Earth and Planetary Science Let-*
 1103 *ters*, 51(2), 445–450.
- 1104 Paulson, A., & Richards, M. A. (2009). On the resolution of radial viscosity struc-
 1105 ture in modelling long-wavelength postglacial rebound data. *Geophysical Jour-*
 1106 *nal International*, 179(3), 1516–1526. Retrieved from [https://doi.org/10](https://doi.org/10.1111/j.1365-246X.2009.04362.x)
 1107 [.1111/j.1365-246X.2009.04362.x](https://doi.org/10.1111/j.1365-246X.2009.04362.x) doi: 10.1111/j.1365-246X.2009.04362.x
- 1108 Phipps Morgan, J., Morgan, W. J., Zhang, Y.-S., & Smith, W. H. (1995). Ob-
 1109 servational hints for a plume-fed, suboceanic asthenosphere and its role in
 1110 mantle convection. *Journal of Geophysical Research: Solid Earth*, 100(B7),
 1111 12753–12767. Retrieved from <https://doi.org/10.1029/95JB00041> doi:
 1112 10.1029/95JB00041
- 1113 Pokorný, J., Čížková, H., & van den Berg, A. (2021). Feedbacks between subduc-
 1114 tion dynamics and slab deformation: Combined effects of nonlinear rheology
 1115 of a weak decoupling layer and phase transitions. *Physics of the Earth and*
 1116 *Planetary Interiors*, 313, 106679. Retrieved from [https://doi.org/10.1016/](https://doi.org/10.1016/j.pepi.2021.106679)
 1117 [j.pepi.2021.106679](https://doi.org/10.1016/j.pepi.2021.106679) doi: 10.1016/j.pepi.2021.106679

- 1118 Pusok, A. E., Stegman, D. R., & Kerr, M. (PREPRINT). The effect of sediments on
 1119 the dynamics and accretionary style of subduction margins. *Solid Earth Dis-*
 1120 *cussions*, 1–30.
- 1121 Raterron, P., Chen, J., Geenen, T., & Girard, J. (2011). Pressure effect on forsterite
 1122 dislocation slip systems: Implications for upper-mantle lpo and low viscosity
 1123 zone. *Physics of the Earth and Planetary Interiors*, 188(1-2), 26–36.
- 1124 Ren, Y., Stutzmann, E., van Der Hilst, R. D., & Besse, J. (2007). Understanding
 1125 seismic heterogeneities in the lower mantle beneath the americas from seismic
 1126 tomography and plate tectonic history. *Journal of Geophysical Research: Solid*
 1127 *Earth*, 112(B1). Retrieved from <https://doi.org/10.1029/2005JB004154>
 1128 doi: 10.1029/2005JB004154
- 1129 Ribe, N. M. (2003). Periodic folding of viscous sheets. *Physical Review E*, 68(3),
 1130 036305. doi: 10.1103/PhysRevE.68.036305
- 1131 Ribe, N. M. (2010). Bending mechanics and mode selection in free subduction: a
 1132 thin-sheet analysis. *Geophysical Journal International*, 180(2), 559–576. Re-
 1133 trieved from <https://doi.org/10.1111/j.1365-246X.2009.04460.x> doi: 10
 1134 .1111/j.1365-246X.2009.04460.x
- 1135 Ribe, N. M., Stutzmann, E., Ren, Y., & Van Der Hilst, R. (2007). Buckling instabil-
 1136 ities of subducted lithosphere beneath the transition zone. *Earth and Planetary*
 1137 *Science Letters*, 254(1), 173–179.
- 1138 Ricard, Y., Doglioni, C., & Sabadini, R. (1991). Differential rotation between litho-
 1139 sphere and mantle: a consequence of lateral mantle viscosity variations. *Jour-*
 1140 *nal of Geophysical Research: Solid Earth*, 96(B5), 8407–8415. Retrieved from
 1141 <https://doi.org/10.1029/91JB00204> doi: 10.1029/91JB00204
- 1142 Ricard, Y., Richards, M., Lithgow-Bertelloni, C., & Le Stunff, Y. (1993). A
 1143 geodynamic model of mantle density heterogeneity. *Journal of Geo-*
 1144 *physical Research: Solid Earth*, 98(B12), 21895–21909. Retrieved from
 1145 <https://doi.org/10.1029/93JB02216> doi: 10.1029/93JB02216
- 1146 Richards, M. A. (1991). Hotspots and the case for a high viscosity lower mantle.
 1147 In *Glacial isostasy, sea-level and mantle rheology* (pp. 571–587). Springer.
 1148 Retrieved from https://doi.org/10.1007/978-94-011-3374-6_27 doi:
 1149 10.1007/978-94-011-3374-6_27
- 1150 Sakamaki, T., Suzuki, A., Ohtani, E., Terasaki, H., Urakawa, S., Katayama, Y., . . .

- 1151 Ballmer, M. D. (2013). Ponded melt at the boundary between the lithosphere
1152 and asthenosphere. *Nature Geoscience*, 6(12), 1041–1044. Retrieved from
1153 <https://doi.org/10.1038/ngeo1982> doi: 10.1038/ngeo1982
- 1154 Schellart, W. P. (2005). Influence of the subducting plate velocity on the geometry
1155 of the slab and migration of the subduction hinge. *Earth and Planetary Sci-*
1156 *ence Letters*, 231(3-4), 197–219. Retrieved from [https://doi.org/10.1016/j](https://doi.org/10.1016/j.epsl.2004.12.019)
1157 [.epsl.2004.12.019](https://doi.org/10.1016/j.epsl.2004.12.019) doi: 10.1016/j.epsl.2004.12.019
- 1158 Schellart, W. P. (2008a). Kinematics and flow patterns in deep mantle and up-
1159 per mantle subduction models: Influence of the mantle depth and slab to
1160 mantle viscosity ratio. *Geochemistry, Geophysics, Geosystems*, 9(3). Re-
1161 trieved from <https://doi.org/10.1111/10.1029/2004JB002970> doi:
1162 10.1029/2004JB002970
- 1163 Schellart, W. P. (2008b). Subduction zone trench migration: Slab driven or
1164 overriding-plate-driven? *Physics of the Earth and Planetary Interiors*, 170(1-
1165 2), 73–88. Retrieved from <https://doi.org/10.1016/j.pepi.2008.07.040>
1166 doi: 10.1016/j.pepi.2008.07.040
- 1167 Schmerr, N. (2012). The gutenbergs discontinuity: Melt at the lithosphere-
1168 asthenosphere boundary. *Science*, 335(6075), 1480–1483. Retrieved from
1169 <https://doi.org/10.1126/science.1215433> doi: 10.1126/science.1215433
- 1170 Sdrolias, M., & Müller, R. (2006). Controls on back-arc basin formation. *Geochem-*
1171 *istry, Geophysics, Geosystems*, 7(4). doi: 10.1029/2005GC001090
- 1172 Sharples, W., Jadamec, M., Moresi, L., & Capitanio, F. (2014). Overriding plate
1173 controls on subduction evolution. *Journal of Geophysical Research: Solid*
1174 *Earth*, 119(8), 6684–6704. Retrieved from [https://doi.org/10.1002/](https://doi.org/10.1002/2014JB011163)
1175 [2014JB011163](https://doi.org/10.1002/2014JB011163) doi: 10.1002/2014JB011163
- 1176 Shephard, G. E., Matthews, K. J., Hosseini, K., & Domeier, M. (2017). On the con-
1177 sistency of seismically imaged lower mantle slabs. *Scientific reports*, 7(1), 1–
1178 17. Retrieved from <https://doi.org/10.1038/s41598-017-11039-w> doi: 10
1179 [.1038/s41598-017-11039-w](https://doi.org/10.1038/s41598-017-11039-w)
- 1180 Sigloch, K., McQuarrie, N., & Nolet, G. (2008). Two-stage subduction history un-
1181 der north america inferred from multiple-frequency tomography. *Nature Geo-*
1182 *science*, 1(7), 458–462.
- 1183 Sigloch, K., & Mihalynuk, M. G. (2013). Intra-oceanic subduction shaped the as-

- 1184 assembly of cordilleran north america. *Nature*, *496*(7443), 50–56. Retrieved from
 1185 <https://doi.org/10.1038/nature12019> doi: 10.1038/nature12019
- 1186 Stegman, D., Farrington, R., Capitanio, F. A., & Schellart, W. P. (2010). A regime
 1187 diagram for subduction styles from 3-d numerical models of free subduction.
 1188 *Tectonophysics*, *483*(1), 29–45. Retrieved from [https://doi.org/10.1016/](https://doi.org/10.1016/j.tecto.2009.08.041)
 1189 [j.tecto.2009.08.041](https://doi.org/10.1016/j.tecto.2009.08.041) doi: 10.1016/j.tecto.2009.08.041
- 1190 Stern, T., Henrys, S. A., Okaya, D., Louie, J. N., Savage, M. K., Lamb, S., ...
 1191 Iwasaki, T. (2015). A seismic reflection image for the base of a tectonic
 1192 plate. *Nature*, *518*(7537), 85–88. Retrieved from [https://doi.org/10.1038/](https://doi.org/10.1038/nature14146)
 1193 [nature14146](https://doi.org/10.1038/nature14146) doi: 10.1038/nature14146
- 1194 Strak, V., & Schellart, W. (2021). Thermo-mechanical numerical modeling of the
 1195 south american subduction zone: A multi-parametric investigation. *Journal*
 1196 *of Geophysical Research: Solid Earth*, *126*(4), e2020JB021527. Retrieved from
 1197 <https://doi.org/10.1029/2020JB021527> doi: 10.1029/2020JB021527
- 1198 Suchoy, L., Goes, S., Maunder, B., Garel, F., & Davies, D. R. (2021). Effects of
 1199 basal drag on subduction dynamics from 2d numerical models. *Solid Earth*,
 1200 *12*(1), 79–93. Retrieved from <https://doi.org/10.5194/se-12-79-2021>
 1201 doi: 10.5194/se-12-79-2021
- 1202 Torii, Y., & Yoshioka, S. (2007). Physical conditions producing slab stagnation:
 1203 Constraints of the clapeyron slope, mantle viscosity, trench retreat, and dip
 1204 angles. *Tectonophysics*, *445*(3), 200–209. Retrieved from [https://doi.org/](https://doi.org/10.1016/j.tecto.2007.08.003)
 1205 [10.1016/j.tecto.2007.08.003](https://doi.org/10.1016/j.tecto.2007.08.003) doi: 10.1016/j.tecto.2007.08.003
- 1206 Tovish, A., Schubert, G., & Luyendyk, B. P. (1978). Mantle flow pressure and the
 1207 angle of subduction: Non-newtonian corner flows. *Journal of Geophysical Re-*
 1208 *search: Solid Earth (1978–2012)*, *83*(B12), 5892–5898.
- 1209 Turcotte, D. L., & Schubert, G. (2002). *Geodynamics*. Cambridge Univ. Press, New
 1210 York.
- 1211 Uyeda, S., & Kanamori, H. (1979). Back-arc opening and the mode of subduction.
 1212 *Journal of Geophysical Research: Solid Earth (1978–2012)*, *84*(B3), 1049–
 1213 1061. Retrieved from <https://doi.org/10.1029/JB084iB03p01049> doi:
 1214 [10.1029/JB084iB03p01049](https://doi.org/10.1029/JB084iB03p01049)
- 1215 Van Der Meer, D. G., Spakman, W., Van Hinsbergen, D. J., Amaru, M. L., &
 1216 Torsvik, T. H. (2010). Towards absolute plate motions constrained by

- 1217 lower-mantle slab remnants. *Nature Geoscience*, 3(1), 36–40. Retrieved
 1218 from <https://doi.org/10.1038/ngeo708> doi: 10.1038/ngeo708
- 1219 Van der Meer, D. G., Van Hinsbergen, D. J., & Spakman, W. (2018). Atlas of
 1220 the underworld: Slab remnants in the mantle, their sinking history, and
 1221 a new outlook on lower mantle viscosity. *Tectonophysics*, 723, 309–448.
 1222 Retrieved from <https://doi.org/10.1016/j.tecto.2017.10.004> doi:
 1223 10.1016/j.tecto.2017.10.004
- 1224 Van der Voo, R., Spakman, W., & Bijwaard, H. (1999). Tethyan subducted
 1225 slabs under india. *Earth and Planetary Science Letters*, 171(1), 7–20. Re-
 1226 trieved from [https://doi.org/10.1016/S0012-821X\(99\)00131-4](https://doi.org/10.1016/S0012-821X(99)00131-4) doi:
 1227 10.1016/S0012-821X(99)00131-4
- 1228 van Hunen, J., Huang, J., & Zhong, S. (2003). The effect of shearing on the on-
 1229 set and vigor of small-scale convection in a newtonian rheology. *Geophysical re-
 1230 search letters*, 30(19).
- 1231 Wang, S., Yu, H., Zhang, Q., & Zhao, Y. (2018). Absolute plate motions relative
 1232 to deep mantle plumes. *Earth and Planetary Science Letters*, 490, 88–99. Re-
 1233 trieved from <https://doi.org/10.1016/j.epsl.2018.03.021> doi: 10.1016/
 1234 j.epsl.2018.03.021
- 1235 Wu, J., Suppe, J., Lu, R., & Kanda, R. (2016). Philippine sea and east asian
 1236 plate tectonics since 52 ma constrained by new subducted slab reconstruc-
 1237 tion methods. *Journal of Geophysical Research: Solid Earth*, 121(6), 4670–
 1238 4741. Retrieved from <https://doi.org/10.1002/2016JB012923> doi:
 1239 10.1002/2016JB012923
- 1240 Yang, T., Moresi, L., Zhao, D., Sandiford, D., & Whittaker, J. (2018). Cenozoic
 1241 lithospheric deformation in northeast asia and the rapidly-aging pacific plate.
 1242 *Earth and Planetary Science Letters*, 492, 1–11. Retrieved from [https://
 1243 doi.org/10.1016/j.epsl.2018.03.057](https://doi.org/10.1016/j.epsl.2018.03.057) doi: 10.1016/j.epsl.2018.03.057
- 1244 Yang, Y., Forsyth, D. W., & Weeraratne, D. S. (2007). Seismic attenuation near
 1245 the east pacific rise and the origin of the low-velocity zone. *Earth and Plane-
 1246 tary Science Letters*, 258(1-2), 260–268. Retrieved from [https://doi.org/10
 1247 .1016/j.epsl.2007.03.040](https://doi.org/10.1016/j.epsl.2007.03.040) doi: 10.1016/j.epsl.2007.03.040
- 1248 Zhang, H., Wang, F., Myhill, R., & Guo, H. (2019). Slab morphology and defor-
 1249 mation beneath izu-bonin. *Nature communications*, 10(1), 1–8. Retrieved

1250 from <https://doi.org/10.1038/s41467-019-09279-7> doi: 10.1038/s41467
1251 -019-09279-7
1252 Zindler, A., & Hart, S. (1986). Chemical geodynamics. *Annual review of earth
1253 and planetary sciences*, 14(1), 493–571. Retrieved from [https://doi.org/
1254 10.1146/annurev.ea.14.050186.002425](https://doi.org/10.1146/annurev.ea.14.050186.002425) doi: 10.1146/annurev.ea.14.050186
1255 .002425